

HERMES: SPATIALLY RESOLVED ALMA IMAGING OF *HERSCHEL*[†]-SELECTED DUSTY STAR-FORMING GALAXIES

R. S. BUSSMANN¹, D. RIECHERS¹, A. FIALKOV², C. HAYWARD^{3,4}, A. LOEB⁴, W. COWLEY⁵, C. LACEY⁵, J. BOCK^{6,7}, J. CALANOG⁸, A. COORAY⁸, F. DE BERNARDIS⁸, R. HOPWOOD⁹, S. J. OLIVER¹⁰, I. PÉREZ-FOURNON^{11,12}, I. G. ROSEBOOM^{10,13}, A. J. SMITH¹⁰, L. WANG¹⁰, J. WARDLOW¹⁴

To be submitted to the ApJ

ABSTRACT

The *Herschel* Multi-tiered Extragalactic Survey (HerMES) has identified large numbers of dusty star-forming galaxies (DSFGs) over a wide range in redshift. A detailed understanding of these DSFGs is hampered by the poor spatial resolution of *Herschel*. We present 870 μm 0''.45 imaging obtained in Cycle 0 with the Atacama Large Millimeter/submillimeter Array (ALMA) of a sample of 29 HerMES DSFGs. We identify a total of 62 sources down to the 5σ limit in our ALMA sample ($\sigma \approx 0.2 \text{ mJy}$). Optical or near-infrared imaging indicates that 36 of the ALMA sources experience a significant flux boost from gravitational lensing ($\mu > 1.1$), but only 6 are strongly lensed and show multiple images. We introduce and make use of UVMCMCFIT, a general purpose and publicly available Markov Chain Monte Carlo visibility plane analysis tool to analyze the source properties. Nearly 70% of the *Herschel* sources break down into multiple ALMA counterparts, consistent with previous research indicating that the multiplicity rate is high in bright sources discovered in sub-mm or FIR surveys with poor spatial resolution. The ALMA counterparts to our *Herschel* targets are located much closer to each other than ALMA counterparts to sources found in the LABOCA ECDFS Submillimeter Survey. Hydrodynamical numerical simulations and semi-analytical models both underpredict the excess in number of sources with small separations from each other that is seen in our ALMA sample. Combined with our previous work on brighter *Herschel* sources, the lens models presented here constrain the shape of the intrinsic luminosity function for DSFGs to have a break around 8 mJy with a very steep fall off at higher flux densities. The high multiplicity rate and low projected separations between sources seen in our sample argue in favor of interactions and mergers driving the prodigious emission from the brightest DSFGs.

Keywords: galaxies: evolution — galaxies: fundamental parameters — galaxies: high-redshift

1. INTRODUCTION

Galaxies selected in blind surveys at far-infrared (FIR) or sub-millimeter (sub-mm) wavelengths are generally known as dusty star-forming galaxies (DSFGs). They

are found primarily at $z \sim 2$ (Chapman et al. 2005; Bothwell et al. 2013) (but extend down to $z \sim 1$ and up to $z > 6$; see Messias et al. 2014; Riechers et al. 2013) and represent the most FIR-luminous objects in existence during this epoch. They are signposts of significant over-densities (Daddi et al. 2009; Capak et al. 2011) and likely represent the formative stages of the most massive elliptical galaxies found in the local Universe (e.g., Ivison et al. 2013; Fu et al. 2013). Moreover, they constitute an important component of the overall galaxy population at $z \sim 2$ (e.g., Le Floc'h et al. 2005), when the star-formation rate density in the Universe peaked (e.g., Lilly et al. 1996; Madau et al. 1996).

Our collective understanding of DSFGs is currently taking a dramatic leap forward thanks in large part to the advent of the *Herschel Space Observatory* (*Herschel*; Pilbratt et al. 2010). This has resulted in a revolution in the size and depth of blind surveys at FIR and sub-mm wavelengths. In particular, the *Herschel* Multi-tiered Extragalactic Survey (HerMES; Oliver et al. 2012) and the *Herschel* Astrophysical Terahertz Large Area Survey (H-ATLAS; Eales et al. 2010) together have surveyed $\approx 650 \text{ deg}^2$ at 250 μm , 350 μm , and 500 μm to the confusion limit of *Herschel* ($\sigma \approx 6 - 7 \text{ mJy}$ in each band Nguyen et al. 2010), plus an additional $\approx 350 \text{ deg}^2$ to a level approximately double the confusion limit. A similar effort has been undertaken at longer wavelengths by the South Pole Telescope (SPT; Carlstrom et al. 2011) and

¹ Department of Astronomy, Space Science Building, Cornell University, Ithaca, NY, 14853-6801

² Departement de Physique, Ecole Normale Sup erieure, CNRS, 24 rue Lhomond, Paris, 75005 France

³ TAPIR 350-17, California Institute of Technology, 1200 E. California Boulevard, Pasadena, CA 91125

⁴ Harvard-Smithsonian Center for Astrophysics, 60 Garden Street, Cambridge, MA 02138

⁵ Institute for Computational Cosmology, Department of Physics, University of Durham, South Road, Durham, DH1 3LE, UK

⁶ California Institute of Technology, 1200 E. California Blvd., Pasadena, CA 91125

⁷ Jet Propulsion Laboratory, 4800 Oak Grove Drive, Pasadena, CA 91109

⁸ Dept. of Physics & Astronomy, University of California, Irvine, CA 92697

⁹ Astrophysics Group, Imperial College London, Blackett Laboratory, Prince Consort Road, London SW7 2AZ, UK

¹⁰ Astronomy Centre, Dept. of Physics & Astronomy, University of Sussex, Brighton BN1 9QH, UK

¹¹ Instituto de Astrofísica de Canarias (IAC), E-38200 La Laguna, Tenerife, Spain

¹² Departamento de Astrofísica, Universidad de La Laguna (ULL), E-38205 La Laguna, Tenerife, Spain

¹³ Institute for Astronomy, University of Edinburgh, Royal Observatory, Blackford Hill, Edinburgh EH9 3HJ, UK

¹⁴ Dark Cosmology Centre, Niels Bohr Institute, University of Copenhagen, Juliane Maries Vej 30, 2100 Copenhagen, Denmark

the Atacama Cosmology Telescope (Swetz et al. 2011). Theoretical expectations based on the redshift distribution and luminosity function of DSFGs suggested that HerMES and H-ATLAS would be efficient tools for discovering strongly lensed DSFGs (e.g., Blain 1996; Negrello et al. 2007). Submillimeter Array (SMA; Ho et al. 2004) imaging at $870\text{ }\mu\text{m}$ with sub-arcsecond resolution has confirmed this, with $\geq 85\%$ of the brightest sources found by *Herschel* ($S_{500} > 100\text{ mJy}$) being gravitationally lensed by an intervening galaxy or group of galaxies along the line of sight (Negrello et al. 2010; Conley et al. 2011; Riechers et al. 2011a; Bussmann et al. 2012; Wardlow et al. 2013; Bussmann et al. 2013). Sources discovered in SPT surveys have also been shown to have a high probability of being strongly lensed (Vieira et al. 2013; Hezaveh et al. 2013). However, statistical models significantly over-predict the median magnification factor experienced by a *Herschel* DSFG of a given S_{500} (Bussmann et al. 2013). This could indicate a deficiency in our understanding of the bright end of the intrinsic DSFG luminosity function.

We here present Atacama Large Millimeter/submillimeter Array (ALMA) Cycle 0 imaging at $870\text{ }\mu\text{m}$ of a sample of 29 HerMES DSFGs. Three aspects of our dataset make it unique. First, the sample occupies a distinct regime in flux density between the brightest *Herschel* DSFGs (almost all of which are lensed) and much fainter DSFGs found in ground-based surveys (most of which are expected to be unlensed; e.g., Hodge et al. 2013). Second, the ALMA images are extremely sensitive ($\sigma \approx 0.2\text{ mJy}$) and all 29 HerMES DSFGs are detected (such is not the case in previous similar studies with shallower imaging; e.g., Smolčić et al. 2012; Barger et al. 2012; Hodge et al. 2013). Third, the typical angular resolutions are $0''.45$ and nearly all sources detected by ALMA are spatially resolved.

We also obtained Gemini-South optical imaging to complement our existing array of ancillary multi-wavelength imaging. We use those data in this paper to identify lensing galaxies which are typically early-types with little on-going star-formation and therefore very weak sub-mm emission.

In Section 2, we characterize our sample and present our ALMA and Gemini-South imaging. Section 3 presents model fitting methodology and model fits to all ALMA sources (lensed and unlensed) using UVMCMCFIT, a publicly available¹⁵ modified version of the visibility plane lens modeling software used in Bussmann et al. (2012, 2013). Results on the effect of lensing on the observed properties of the *Herschel* DSFGs in our sample as well as the multiplicity rate and typical angular separation between sources after delensing the ALMA sources appear in Section 4. We scrutinize statistical predictions for μ_{870} as a function of S_{870} and discuss implications for the bright end of the DSFG luminosity function in Section 5. Finally, we present our conclusions in Section 6.

Throughout this paper, we assume a flat cosmology with $H_0 = 69\text{ km s}^{-1}\text{ Mpc}^{-1}$, $\Omega_{m0} = 0.29$ (Hinshaw et al. 2013).

2. DATA

In this section, we describe the selection of our *Herschel* DSFG sample, present our ALMA high-spatial resolution imaging of thermal dust emission, and present Gemini-S optical imaging that we use to identify intervening galaxies along the line of sight.

2.1. Selection of DSFG Sample

The starting point for the sample selection is source extraction and photometry. Sources are detected using the STARNFINDER code (Diolaiti et al. 2000) on the $250\text{ }\mu\text{m}$ *Herschel* Spectral and Photometric Imaging Receiver (SPIRE; Griffin et al. 2010) images. Photometry is obtained from the HerMES XID pipeline (Roseboom et al. 2010), which allocates flux density based on the $250\text{ }\mu\text{m}$ position priors from STARNFINDER.

Our sample includes 29 DSFGs drawn from five independent fields in HerMES totaling 55 deg^2 that are accessible to ALMA and have SPIRE sensitivity that reaches the confusion limit. The sample is selected primarily on the basis of S_{500} and covers a range of $20 < S_{500}/(\text{mJy}) \lesssim 100$. Additional selection criteria based on the S_{500}/S_{350} and S_{350}/S_{250} colors lead to the sample being split roughly evenly between “blue” (typically implying $z < 2$) and “green” ($z = 2 - 3.5$) SPIRE colors. We caution that redshifts based strictly on SPIRE colors are uncertain due to the degeneracy between dust temperature and redshift as well as the fact that the multiplicity rate is high in our sample. It is not clear that the colors of each individual ALMA counterpart are the same as the summed colors seen by *Herschel*. Low redshift contaminants to our sample ($z < 0.1$) are trivially removed by searching for spatially resolved counterparts in SDSS imaging. There is also a small contamination from blazars, which are non-thermal emitters and are easily identified and excised from the sample using data from the NVSS or the Very Large Array Faint Images of the Radio Sky at Twenty-Centimeters survey (FIRST; Becker et al. 1995).

Figure 1 shows that the ALMA sample is set clearly apart from the very bright *Herschel* DSFGs that are selected to have $S_{500} > 100\text{ mJy}$ and have been shown to be almost entirely lensed DSFGs (Negrello et al. 2010; Wardlow et al. 2013; Bussmann et al. 2013). In contrast, the sample in this paper should include a more diverse mix of lensed and unlensed DSFGs. On the other hand, this sample is selected from a survey with an area that is 200 times larger than that of ALESS. It is no surprise then, that the median S_{500} in our sample is ~ 3.5 times brighter than the median S_{500} in ALESS. Our ALMA sample opens a new window of discovery space on the bright end of the DSFG luminosity function.

In detail, two of the sources in the ALMA sample (HXMM01 and HXMM02) overlap with the “confirmed lensed” sample in Wardlow et al. (2013) as well as with the SMA sample in Bussmann et al. (2013). A further 8 appear in the “Supplementary sample” in Wardlow et al. (2013). The remainder have $S_{500} < 80\text{ mJy}$ and thus do not appear in Wardlow et al. (2013).

Table 1 provides reference data for the ALMA sample, including centroid positions measured from the ALMA $870\text{ }\mu\text{m}$ imaging (see section 2.2).

2.2. ALMA Observations

¹⁵ <https://github.com/sbussmann/uvmcmcfit>

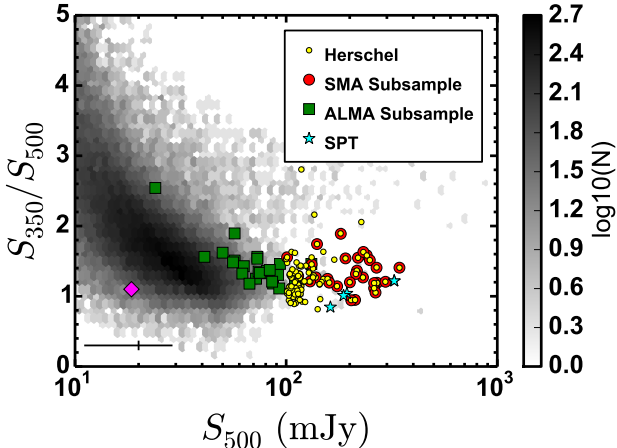


Figure 1. *Herschel*/SPIRE photometry of all galaxies in the H-ATLAS phase I catalog with $S/N > 3$ at $250\text{ }\mu\text{m}$, $350\text{ }\mu\text{m}$, and $500\text{ }\mu\text{m}$ (grayscale). The sample of HerMES sources in this paper are shown with green squares (the “ALMA sample”). The very bright *Herschel* DSFGs from Bussmann et al. (2013) (the “SMA sample”) are shown by red circles, and the overall sample of candidate lensed *Herschel* DSFGs are highlighted by yellow circles. Lensed SMGs discovered by the SPT that have published lens models are represented by cyan stars (Hezaveh et al. 2013). A magenta diamond shows the location in this diagram of the stacked signal from ALESS DSFGs. Representative error bars are shown in the lower left corner. The ALMA sample fills the gap in $500\text{ }\mu\text{m}$ flux density space between SMA/SPT and ALESS samples.

ALMA data were obtained during Cycle 0 over a period from 2012 June to 2012 December (Program 2011.0.000539.S; PI: D. Riechers). The observations were carried out in good $870\text{ }\mu\text{m}$ weather conditions which resulted in typical system temperatures of $T_{\text{sys}} \sim 130\text{ K}$ and phase fluctuations of $\sim 10\text{ deg}$. Each target was observed until an rms noise level of $\sigma \approx 0.2\text{ mJy}$ was achieved. This typically required 10 minutes of on-source integration time. For the observations targeting the CDFS, Elais-S, and COSMOS fields, the weather was of sufficient quality to reach $\sigma \approx 0.14\text{ mJy}$. The number of antennas used varied from 15 to 25. The antennas were configured with baseline lengths of 20 m to 400 m, providing a synthesized beamsize of $\approx 0''.45$ FWHM while ensuring that no flux was resolved out by the interferometer. When possible, track-sharing of multiple targets in a single track was used to optimize the uv coverage.

The quasars J0403–360, J2258–279, B0851+202, and J2258–279 were used for bandpass and pointing calibration. The quasars J0403–360, J0106–405, J0519–454, J1008+063, and J0217+017 were used for amplitude and phase gain calibration. The following solar system objects were used for absolute flux calibration: Callisto (CDFS targets), Neptune (XMM targets), Titan (COSMOS targets) and Uranus (ADFS and XMM targets). For ElaisS1, no solar system object was observed. Instead, J2258–279 was used for absolute flux calibration, with the flux fixed according to a measurement made two days prior to the observations of ElaisS1.

All observations were conducted with the correlator in “Frequency Domain Mode”, providing a total usable bandwidth of 7.5 GHz with spectral windows centered on 335.995 GHz, 337.995 GHz, 345.995 GHz, 347.996 GHz. We searched for evidence of serendipitous spectral lines but found none (typical sensitivity is $\sigma \approx 8\text{ mJy beam}^{-1}$ in 15 km sec^{-1} bins).

We used the Common Astronomy Software Applications (CASA, version 4.2.1) package to investigate the quality of the reduced data provided by the North American ALMA Science Center (NAASC). Overall, the quality of the processed data from the NAASC was very high. We achieved a significant improvement in the case of the ADFS and XMM targets by excluding datasets with moderate T_{sys} and poor phase fluctuations. For a handful of targets with peak signal-to-noise ratio (S/N) greater than 20, we obtained a $\approx 10\%$ improvement in S/N by using the CASA SELFCAL task to improve the phase gain corrections. Finally, we updated the absolute flux calibration to use the Butler-JPL-Horizons 2012 solar system models.

For imaging, we used the CASA CLEAN task with Briggs weighting and robust = +0.5 to achieve an optimal balance between sensitivity and spatial resolution. We selected the multi-frequency synthesis option to optimize uv coverage. We designed custom masks for each target in CASA to ensure that only regions with high S/N were considered during the cleaning process.

Figure 2 presents our ALMA images (colorscale) in comparison to the *Herschel* SPIRE images (black-white contours) originally used to select the targets and noted in each panel as either $250\text{ }\mu\text{m}$ or $350\text{ }\mu\text{m}$. Each panel is centered on the phase center of the ALMA observations of that target and a white circle traces the FWHM of the primary beam of an ALMA 12 m antenna at $870\text{ }\mu\text{m}$. A white dashed box represents the region of each image that is shown in greater detail in Figure 3.

In most targets, the peak of the SPIRE map is spatially coincident with the location of the ALMA sources. In one case where two ALMA sources are separated by $\approx 10''$ (ADFS02), the elongation in the SPIRE $250\text{ }\mu\text{m}$ map is consistent with the angular separation of the two ALMA counterparts. Otherwise, the SPIRE imaging is consistent with a single component located at the centroid of the ALMA sources. This result is not a surprise, given the typical angular separation of the ALMA sources ($\lesssim 5''$) and the FWHM of the SPIRE beam at $250\text{ }\mu\text{m}$ ($18.1''$).

2.3. Gemini-South Imaging

Optical imaging observations using the Gemini Multi-Object Spectrograph-South (GMOS-S; Hook et al. 2004) were conducted in queue mode during the 2013B semester as part of program GS-2013B-Q-77 (PI: R. S. Bussmann). The goal of the program is to use shallow u , g , r , i , and z imaging to identify structure at $z < 1$ and determine which of the ALMA sources are affected by gravitational lensing. Nearly half of the ALMA sources lie in regions with existing deep optical imaging thanks to the extensive HerMES multi-wavelength dataset — these were excluded from our Gemini-S program. The remaining targets are: ADFS01, ADFS02, ADFS03, ADFS04, ADFS05, ADFS06, ADFS07, ADFS_M0, ElaisS1, XMM02, XMM05, XMM101, XMM108, XMM109, and XMM115. Each of these targets were observed for a total of 9 minutes of on-source integration time in each of u , g , r , i , and z . The observations were obtained during dark time in with adequate seeing conditions (image quality = 85% $\approx 1.1''$).

The data were reduced using the standard IRAF Gem-

ini GMOS reduction routines, following the standard GMOS-S reduction steps in the example taken from the Gemini observatory webpage¹⁶.

We used the Sloan Digital Sky Survey (SDSS) or the 2 Micron All Sky Survey (2MASS) to align the Gemini-S images to a common astrometric frame of reference. This

imposes an rms uncertainty in the absolute astrometry of 0''.2 and 0''.4 for SDSS and 2MASS, respectively. The astrometrically calibrated Gemini-S images served as the basis for aligning higher resolution, smaller field-of-view imaging from *HST* or Keck that were originally presented in Calanog et al. (2014).

Table 1
Observed positions and flux densities of ALMA sources. Uncertainties in flux densities do not include absolute calibration uncertainty of $\approx 10\%$.

IAU address ^a	Short name	RA ₈₇₀ (J2000)	Dec ₈₇₀ (J2000)	S ₂₅₀ (mJy)	S ₃₅₀ (mJy)	S ₅₀₀ (mJy)	S ₈₇₀ (mJy)	Lens Grade
J045057.5-531654	ADFS01	04:50:57.715	-53:16:54.42	138 \pm 6	114 \pm 6	73 \pm 6	10.41 \pm 0.44	—
—	Source0	04:50:57.610	-53:16:55.09	—	—	—	6.68 \pm 0.28	C
—	Source1	04:50:57.805	-53:16:56.96	—	—	—	1.98 \pm 0.18	C
—	Source2	04:50:57.741	-53:16:54.54	—	—	—	1.75 \pm 0.26	C
J045026.5-524127	ADFS02	04:50:27.453	-52:41:25.41	88 \pm 6	81 \pm 6	50 \pm 6	10.39 \pm 0.42	—
—	Source0	04:50:27.092	-52:41:25.62	—	—	—	5.56 \pm 0.23	C
—	Source1	04:50:27.806	-52:41:25.10	—	—	—	4.83 \pm 0.35	X
J044946.9-525424	ADFS03	04:49:46.448	-52:54:26.95	115 \pm 6	61 \pm 6	24 \pm 6	13.39 \pm 0.49	—
—	Source0	04:49:46.603	-52:54:23.66	—	—	—	7.50 \pm 0.24	X
—	Source1	04:49:46.301	-52:54:30.26	—	—	—	3.84 \pm 0.27	X
—	Source2	04:49:46.280	-52:54:26.06	—	—	—	2.06 \pm 0.30	X
J044103.8-531240	ADFS04	04:41:03.942	-53:12:41.01	96 \pm 6	86 \pm 6	57 \pm 6	14.94 \pm 0.33	—
—	Source0	04:41:03.866	-53:12:41.33	—	—	—	8.65 \pm 0.23	X
—	Source1	04:41:04.000	-53:12:40.10	—	—	—	3.53 \pm 0.18	X
—	Source2	04:41:03.912	-53:12:42.09	—	—	—	2.76 \pm 0.16	X
J043619.3-552425	ADFS05	04:36:19.702	-55:24:25.01	110 \pm 6	102 \pm 6	87 \pm 6	15.29 \pm 0.37	—
—	Source0	04:36:19.706	-55:24:24.41	—	—	—	7.02 \pm 0.42	X
—	Source1	04:36:19.698	-55:24:25.27	—	—	—	8.27 \pm 0.53	X
J043340.5-540337	ADFS06	04:33:40.450	-54:03:39.51	76 \pm 6	90 \pm 6	72 \pm 6	17.94 \pm 0.50	—
—	Source0	04:33:40.455	-54:03:40.29	—	—	—	9.07 \pm 0.27	C
—	Source1	04:33:40.501	-54:03:40.05	—	—	—	6.08 \pm 0.32	C
—	Source2	04:33:40.472	-54:03:38.33	—	—	—	2.79 \pm 0.27	C
J044153.9-540350	ADFS07	04:41:53.880	-54:03:53.48	80 \pm 6	103 \pm 6	93 \pm 6	32.36 \pm 0.64	A
J043829.7-541831	ADFS_M0	04:38:30.883	-54:18:29.38	57 \pm 6	78 \pm 5	75 \pm 6	20.59 \pm 0.48	—
—	Source0	04:38:30.780	-54:18:31.79	—	—	—	14.00 \pm 0.40	C
—	Source1	04:38:30.970	-54:18:26.60	—	—	—	6.59 \pm 0.28	C
J032752.0-290908	CDFS_M0	03:27:52.011	-29:09:10.40	28 \pm 7	84 \pm 6	85 \pm 6	33.16 \pm 0.45	—
—	Source0	03:27:52.002	-29:09:12.07	—	—	—	13.07 \pm 0.40	A
—	Source1	03:27:52.002	-29:09:09.65	—	—	—	14.26 \pm 0.22	C
—	Source2	03:27:52.025	-29:09:12.14	—	—	—	5.83 \pm 0.11	X
J033210.8-270535	CDFS_M1	03:32:10.840	-27:05:34.18	73 \pm 6	86 \pm 6	85 \pm 6	13.12 \pm 0.25	—
—	Source0	03:32:10.905	-27:05:32.87	—	—	—	10.54 \pm 0.24	C
—	Source1	03:32:10.729	-27:05:36.22	—	—	—	2.58 \pm 0.11	C
J033317.9-280907	ECDFS02	03:33:18.017	-28:09:07.52	96 \pm 6	90 \pm 6	63 \pm 6	14.13 \pm 0.25	—
—	Source0	03:33:18.006	-28:09:07.55	—	—	—	9.30 \pm 1.20	X
—	Source1	03:33:18.032	-28:09:07.39	—	—	—	4.83 \pm 1.26	X
J100144.1+025712	COS01	10:01:44.182	+02:57:12.47	91 \pm 6	100 \pm 6	74 \pm 6	12.82 \pm 0.39	A
J100056.6+022014	COS02	10:00:57.180	+02:20:12.70	71 \pm 6	64 \pm 6	41 \pm 6	10.37 \pm 0.51	—
—	Source0	10:00:56.946	+02:20:17.35	—	—	—	3.31 \pm 0.16	X
—	Source1	10:00:57.565	+02:20:11.26	—	—	—	2.26 \pm 0.19	X
—	Source2	10:00:56.855	+02:20:08.93	—	—	—	1.54 \pm 0.23	X
—	Source3	10:00:57.274	+02:20:12.66	—	—	—	1.45 \pm 0.18	X
—	Source4	10:00:57.400	+02:20:10.83	—	—	—	1.80 \pm 0.33	X
J003823.6-433707	ElaisS1	00:38:23.587	-43:37:04.15	114 \pm 6	101 \pm 6	76 \pm 6	17.20 \pm 0.44	—
—	Source0	00:38:23.762	-43:37:06.10	—	—	—	8.85 \pm 0.21	C
—	Source1	00:38:23.482	-43:37:05.56	—	—	—	3.76 \pm 0.19	C
—	Source2	00:38:23.313	-43:36:58.97	—	—	—	2.84 \pm 0.23	C
—	Source3	00:38:23.803	-43:37:10.46	—	—	—	1.75 \pm 0.20	X
J022016.5-060143	XMM01	02:20:16.609	-06:01:43.18	180 \pm 7	192 \pm 8	132 \pm 7	25.09 \pm 0.51	—
—	Source0	02:20:16.648	-06:01:41.93	—	—	—	13.77 \pm 0.34	C
—	Source1	02:20:16.571	-06:01:44.56	—	—	—	10.56 \pm 0.37	C
—	Source2	02:20:16.609	-06:01:40.72	—	—	—	0.76 \pm 0.32	C
J022201.6-033340	XMM02	02:22:01.616	-03:33:41.40	107 \pm 7	108 \pm 8	81 \pm 7	11.57 \pm 0.56	—
—	Source0	02:22:01.592	-03:33:39.42	—	—	—	8.45 \pm 0.38	C
—	Source1	02:22:01.629	-03:33:43.58	—	—	—	3.12 \pm 0.41	X
J022548 -041750	XMM03	02:25:47.942	-04:17:50.80	106 \pm 7	119 \pm 8	92 \pm 7	14.73 \pm 0.35	C
J021853.1-063325	XMM04	02:18:53.111	-06:33:24.65	89 \pm 7	83 \pm 7	56 \pm 7	7.25 \pm 0.44	—
—	Source0	02:18:53.118	-06:33:24.19	—	—	—	5.46 \pm 0.30	C
—	Source1	02:18:53.095	-06:33:25.21	—	—	—	1.78 \pm 0.37	C
J023006.0-034152	XMM05	02:30:05.950	-03:41:53.07	102 \pm 7	110 \pm 8	81 \pm 7	16.34 \pm 0.37	C
J021830.5-053124	XMM06	02:18:30.673	-05:31:31.75	92 \pm 7	122 \pm 8	113 \pm 7	62.06 \pm 0.57	A
J022135.1-062617	XMM16	02:21:34.891	-06:26:17.87	121 \pm 7	132 \pm 8	110 \pm 7	18.58 \pm 0.41	C

¹⁶ <http://www.gemini.edu/sciops/data-and-results/processing-software/getting-started#gmos>

Table 1 — *Continued*

IAU address ^a	Short name	RA ₈₇₀ (J2000)	Dec ₈₇₀ (J2000)	S_{250} (mJy)	S_{350} (mJy)	S_{500} (mJy)	S_{870} (mJy)	Lens Grade
J022250.5-032410	XMM101	02:22:50.573	-03:24:12.35	97 ± 7	82 ± 7	62 ± 7	8.77 ± 0.24	C
J021942.7-052436	XMM102	02:19:42.783	-05:24:34.84	85 ± 7	79 ± 7	67 ± 7	14.21 ± 0.61	—
—	Source0	02:19:42.629	-05:24:37.11	—	—	—	5.15 ± 0.32	X
—	Source1	02:19:42.838	-05:24:35.11	—	—	—	3.31 ± 0.39	X
—	Source2	02:19:42.769	-05:24:36.48	—	—	—	2.88 ± 0.22	X
—	Source3	02:19:42.682	-05:24:36.82	—	—	—	1.94 ± 0.37	X
—	Source4	02:19:42.955	-05:24:32.22	—	—	—	0.94 ± 0.18	X
J021918.4-031051	XMM108	02:19:18.417	-03:10:51.35	91 ± 7	104 ± 8	86 ± 7	29.16 ± 0.58	A
J022944.7-034110	XMM109	02:29:44.740	-03:41:09.57	90 ± 7	100 ± 7	75 ± 7	23.13 ± 0.41	—
—	Source0	02:29:44.701	-03:41:09.29	—	—	—	19.62 ± 0.27	C
—	Source1	02:29:44.793	-03:41:09.92	—	—	—	3.51 ± 0.30	C
J021841.5-035002	XMM110	02:18:41.613	-03:50:03.70	128 ± 7	112 ± 7	73 ± 7	10.13 ± 0.43	—
—	Source0	02:18:41.520	-03:50:04.72	—	—	—	6.31 ± 0.34	X
—	Source1	02:18:41.700	-03:50:02.57	—	—	—	3.81 ± 0.25	C
J022021.7-015328	XMM115	02:20:21.756	-01:53:30.92	144 ± 7	137 ± 8	93 ± 11	17.61 ± 0.49	C
J022029.2-064845	XMM119	02:20:29.140	-06:48:46.49	120 ± 7	115 ± 8	84 ± 7	14.46 ± 0.37	—
—	Source0	02:20:29.195	-06:48:48.02	—	—	—	8.47 ± 0.30	C
—	Source1	02:20:29.079	-06:48:44.86	—	—	—	5.98 ± 0.18	C
J022205.4-070728	XMM124	02:22:05.362	-07:07:28.10	137 ± 7	108 ± 7	57 ± 7	2.75 ± 0.14	X

^a IAU name = 1HerMES S250 + IAU address

3. MODEL FITS

3.1. Model Fitting Methodology

An interferometer measures visibilities at discrete points in the *uv* plane. This is why pixel-to-pixel errors in the inverted and deconvolved surface brightness map of an astronomical source are correlated. The best way to deal with this situation is to compare model and data visibilities rather than surface brightness maps. The methodology used in this paper is similar in many aspects to that used in Bussmann et al. (2012), who presented the first lens model derived from a visibility-plane analysis of interferometric imaging of a strongly lensed DSFG discovered in wide-field submm surveys as well as Bussmann et al. (2013), who extended this work to a statistically significant sample of 30 objects. It also bears some resemblance to the method used in Hezaveh et al. (2013), who undertake lens modeling of interferometric data in the visibility plane. We summarize important information on the methodology here, taking care to highlight where any differences occur between this work and that of our previous efforts.

We created and made publicly available custom software, called UVMCMCFIT, that is capable of modeling all of the ALMA sources in this paper efficiently and reliably.

Sources are assumed to be elliptical Gaussians that are parameterized by the following six free parameters: the position of the source (relative to the primary lens if a lens is present) ($\Delta\alpha_s$ and $\Delta\delta_s$), the total intrinsic flux density (S_{in}), the effective radius intermediate axis length ($r_s = \sqrt{a_s b_s}$), the axial ratio ($q_s = b_s/a_s$), and the position angle (ϕ_s , degrees east of north). The use of an elliptical Gaussian represents a simplification from the Sérsic profile (Sersic 1968) that is justified based on the relatively weak constraints on the Sérsic index found in our previous work (Bussmann et al. 2012, 2013).

When an intervening galaxy (or group of galaxies) is present along the line of sight, UVMCMCFIT accounts for the deflection of light caused by this structure using a

simple ray-tracing routine that is adopted from a Python routine written by A. Bolton¹⁷. This represents a significant difference from Bussmann et al. (2012) and Bussmann et al. (2013), where we used the publicly available GRAVELENS software (Keeton 2001) to map emission from the source plane to the image plane for a given lensing mass distribution. GRAVELENS has a wide range of lens mass profiles as well as a sophisticated algorithm for mapping source-plane emission to the image-plane, but it also comes with a significant input/output penalty that makes parallel computing prohibitively expensive. The use of pure-Python code for tracing the deflection of light rays is a critical component of making UVMCMCFIT computationally feasible.

In UVMCMCFIT, lens mass profiles are represented by N_{lens} singular isothermal ellipsoid (SIE) profiles, where N_{lens} is the number of lensing galaxies found from the best available optical or near-IR imaging (a multitude of evidence supports the SIE as a reasonable choice; for a recent review, see Treu 2010). Each SIE is fully described by the following five free parameters: the position of the lens relative to the arbitrarily chosen “image center” based on the ALMA 870 μm emission and any lensing galaxies seen in the optical or near-IR ($\Delta\alpha_{\text{lens}}$ and $\Delta\delta_{\text{lens}}$; these can be compared with the position of the optical or near-IR counterpart relative to the “image center”: $\Delta\alpha_{\text{NIR}}$ and $\Delta\delta_{\text{NIR}}$), the mass of the lens (parameterized in terms of the intermediate axis angular Einstein radius, θ_E), the axial ratio of the lens ($q_{\text{lens}} = b_{\text{lens}}/a_{\text{lens}}$), and the position angle of the lens (ϕ_{lens} ; degrees east of north). Unless otherwise stated, when optical or near-IR imaging suggests the presence of additional lenses (see Figure 3), we estimate centroids for each lens by-eye and fix the positions of the additional lenses with respect to the primary lens. Each additional lens thus has 3 free parameters: θ_E , q_{lens} , and ϕ_{lens} . We assume secondary, tertiary, etc., lenses are located at the same redshift as the primary lens.

The total number of free parameters for any given system is $N_{\text{free}} = 5 + 3 \times (N_{\text{lens}} - 1) + 6 * N_{\text{source}}$, where

¹⁷ http://www.physics.utah.edu/~bolton/python_lens_demo/

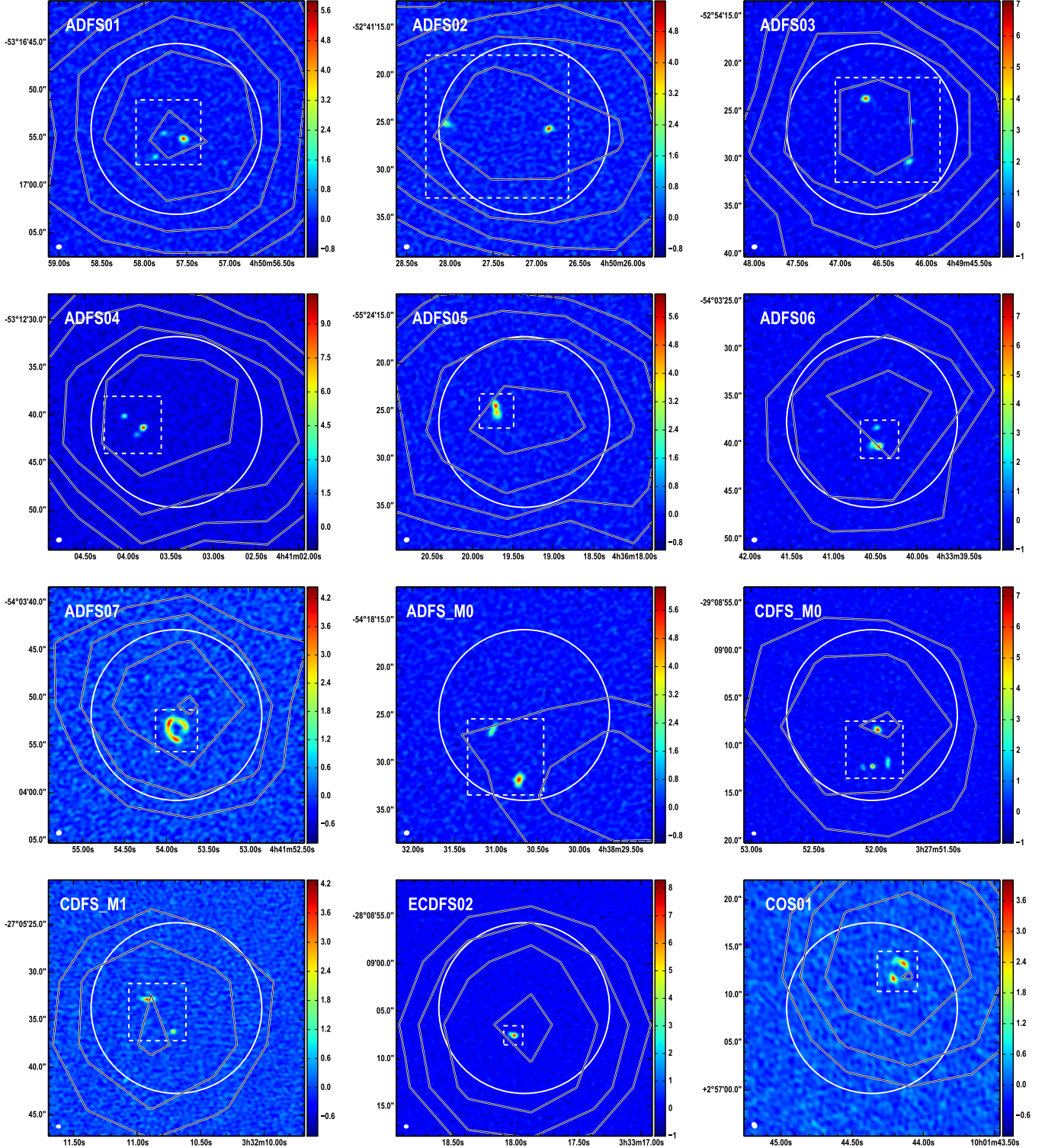
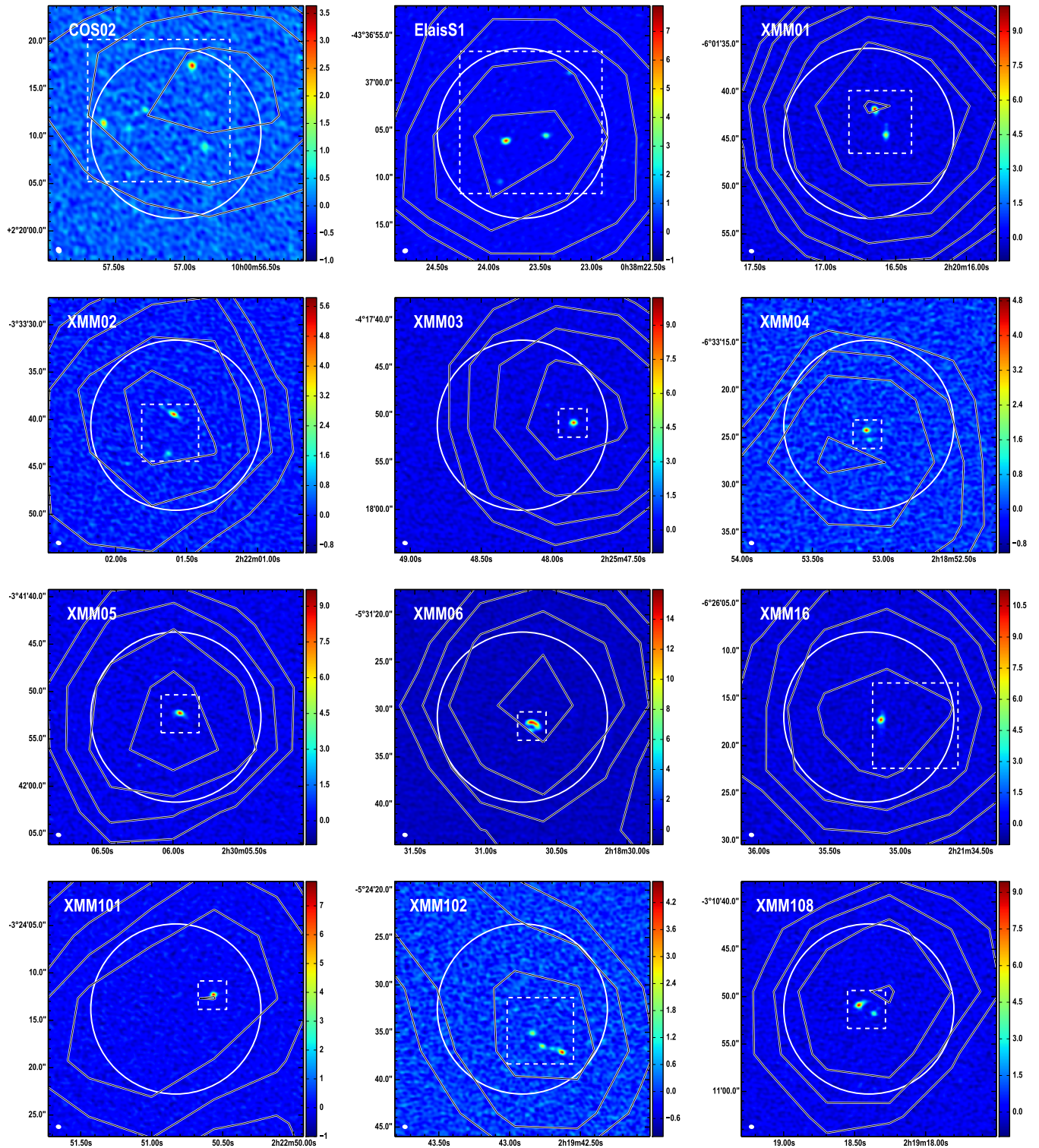


Figure 2. ALMA 870 μm images (color scale, units of mJy/beam) of HerMES DSFGs. Contours (black and white) trace 250 μm emission from *Herschel*. The FWHM size of the ALMA synthesized beam is shown in the lower left corner of each panel. A solid white circle shows the FWHM size of the primary beam. Dashed squares identify the regions of each image that are shown in greater detail in Figure 3.

**Figure 2.** Continued.

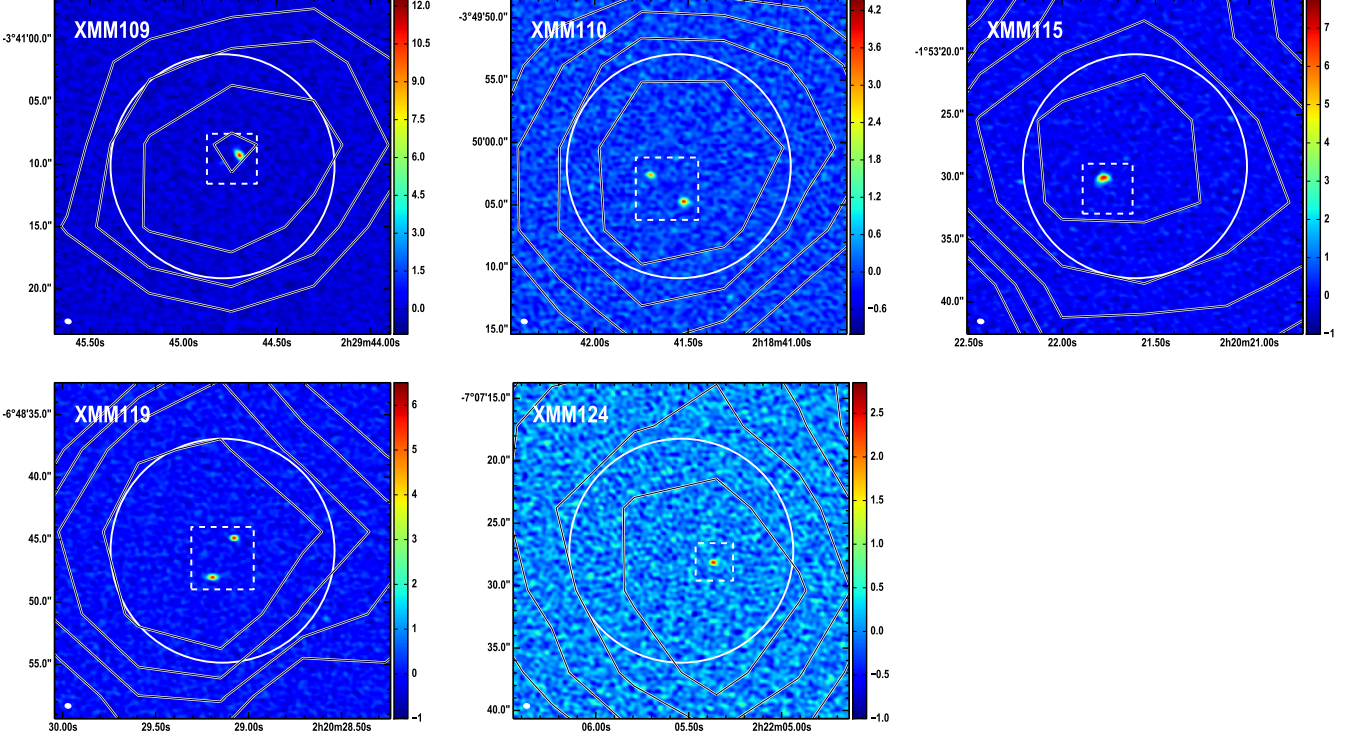


Figure 2. Continued.

N_{source} is the number of Sérsic profiles used.

We use uniform priors for all model parameters. The prior on the position of the lenses covers $\pm 0''.6$ ($1''.0$) in both RA and Dec, a value that reflects the 1σ absolute astrometric solution between the ALMA and optical/near-IR images of $0''.2$ ($0''.4$) for SDSS-based (2MASS-based) astrometric calibration. In section 3.2, we discuss the level of agreement between the astrometry from the images and the astrometry from the lens modeling on an object-by-object basis. For θ_E , the prior covers $0''.1$ – $6''$. The axial ratios of the lenses and sources are restricted to be $q_{\text{lens}} > 0.3$ and $q_s > 0.2$. No prior is placed on the position angle of the lens or source. The intrinsic flux density for any source is allowed to vary from 0.1 mJy to the total flux density observed by the ALMA (we ensure that the posterior PDF of the intrinsic flux density shows no signs of preferring a value lower than 0.1 mJy). The source position is allowed to vary over any reasonable range necessary to fit the data (typically, this is ± 1 – $2''$). The effective radius is allowed to vary from $0''.01$ – $1''.5$.

The surface brightness map generated as part of UVMCMCFIT is then converted to a “simulated visibility” dataset (V_{model}) in much the same way as MIRIAD’s UVMODEL routine. Indeed, the code used in UVMCMCFIT is a direct Python port of UVMODEL (the use of UVMODEL itself is not possible for the same reason as GRAVELENS: constant input/output makes parallel computing prohibitively expensive). UVMCMCFIT computes the Fourier transform of the surface brightness map and samples the resulting visibilities in a way that closely matches the sampling of the actual observed ALMA visibility dataset (V_{ALMA}).

The quality of fit for a given set of model parameters is determined from the maximum likelihood estimate MLE

according to the following equation:

$$MLE = \sum_{u,v} \frac{|V_{\text{ALMA}} - V_{\text{model}}|^2}{\sigma^2} + \log(2\pi\sigma^2) \quad (1)$$

where σ is the 1σ uncertainty level for each visibility and is determined from the scatter in the visibilities within a single spectral window (this is a natural weighting scheme).

We use EMCEE (Foreman-Mackey et al. 2013) to sample the posterior probability density function (PDF) of our model parameters. EMCEE is a Markov chain Monte Carlo (MCMC) code that uses an affine-invariant ensemble sampler to obtain significant performance advantages over standard MCMC sampling methods (Goodman & Weare 2010).

We employ a “burn-in” phase with 512 walkers and 500–1000 iterations (i.e., $\approx 250,000$ – $500,000$ samplings of the posterior PDF) to identify the best-fit model parameters. This position then serves as the basis to initialize the “final” phase with 512 walkers and 10 iterations (i.e., 5,120 samplings of the posterior PDF) to determine uncertainties on the best-fit model parameters.

During each MCMC iteration, we also measure the magnification factor at $870\mu\text{m}$, μ_{870} , for each source. This is done simply by taking the ratio of the total flux density in the lensed image of the model (S_{out}) to the total flux density in the unlensed, intrinsic source model (S_{in}). The use of an aperture when computing μ_{870} is important when source profiles are used with significant flux at large radii (e.g., some types of Sérsic profiles). For an elliptical Gaussian, such a step is unnecessary (note that we did test this and found only $\approx 10\%$ difference between μ_{870} computed with and without an aperture).

The best-fit value and 1σ uncertainty on μ_{870} are drawn from the posterior PDF, as with the other parameters of the model.

3.2. Individual Model Fits

In this section, we present our model fits (as shown in Figure 3) and describe each source in detail.

ADFS01: Three sources are detected by ALMA, each of which is weakly lensed by a bright foreground galaxy seen in the *HST* image. Alternative scenarios involving strong lensing can be ruled out by the location of the lens: $\approx 2 - 3''$ north of the centroid of the ALMA sources (the rms error in the astrometry is set from 2MASS at a level of $\approx 0''.4$) as well as the unusual location and fluxes of the ALMA sources relative to each other. We assume an Einstein radius of $0''.5$ and fix the position angle of the lens to be between 40–50 degrees to match the orientation seen in the *HST* image. Larger Einstein radii can be ruled out by the absence of counter images north of the lens.

ADFS02: Two sources are detected by ALMA, both of which are weakly lensed by a foreground galaxy in the *HST* image. The ALMA sources have the largest separation of any in our sample overall: $\approx 10''$. We assume an Einstein radius of $1''.5$ for the foreground lens as a “maximal lensing” scenario. This results in magnification factors of $\mu_{870} = 2.3 \pm 0.1$ and $\mu_{870} = 1.2 \pm 0.1$ for the two sources. Our constraints on the true Einstein radius of the lens are weak, so these values for μ_{870} should be regarded as upper limits.

ADFS03: Three sources are detected by ALMA, none of which appear to be lensed (the closest bright *HST* source is located $\approx 13''$ away from the ALMA sources).

ADFS04: Three sources are detected by ALMA. In this paper, we have assumed that all three are unlensed. There is a group of three sources detected in our Gemini-S optical imaging located $\approx 7''$ east of the ALMA sources. This distance is so large that plausible mass ranges for the Gemini-S sources would imply at most a factor of 1.1–1.2 boost in the apparent flux densities of the ALMA sources.

ADFS05: Two sources are detected by ALMA. The nearest possible lens is located $\approx 8''$ from the ALMA sources, indicating that lensing is likely to be irrelevant in this system. The two ALMA sources are similarly bright ($S_{870} = 8.27 \pm 0.53$ mJy and $S_{870} = 9.07 \pm 0.27$ mJy) and separated by $\approx 0''.8$, corresponding to a projected physical distance of ≈ 6 kpc. This distance is typical of the pericentric passage distance in both hydrodynamical simulations of major mergers (e.g., Hayward et al. 2012a) and CO observations of major mergers (e.g., Tacconi et al. 2008; Engel et al. 2010; Riechers et al. 2011b; Ivison et al. 2011). Two plausible scenarios are that ADFS05 represents a major merger that just experienced a first pass or is approaching final coalescence, either of which significantly enhanced star-formation in the system.

ADFS06: Three sources are detected by ALMA, all of which are weakly lensed by a foreground galaxy seen in the *HST* image. We assume an Einstein radius of $0''.5$ for the lens, as values larger than this produce multiple images of the ALMA sources. Based on the brightness of the lens, we consider to be unlikely values for the Einstein radius that are smaller than $0''.5$, so the results we report for this object should be robust.

ADFS07: This is a single source that is strongly lensed by a foreground galaxy seen in the *HST* image. The lensed source is not detected by *HST*. The source is highly elongated ($q_s = 0.31 \pm 0.01$), but fits the data very well. The position of the lens according to the lens model is consistent with the position in the *HST* image given the $0''.4$ fundamental uncertainty due to using the 2MASS system as the fundamental basis for the astrometry.

ADFS_M0: Two sources are detected by ALMA, both of which are weakly lensed by a group of small galaxies detected in the *HST* image. We represent the gravitational potential of the group with a single SIE lens and an Einstein radius of $1''.0$. Values larger than this produce additional counter images that are not seen in the ALMA imaging. We cannot rule out smaller Einstein radii, but we consider these unlikely given the number of sources and their brightness in the *HST* image.

CDFS_M0: This is a complex, very well constrained system. Two sources are detected by ALMA: one is strongly lensed and the other is weakly lensed. In addition, the lens is detected by ALMA (this is one of two sources in the entire ALMA sample that is unresolved by ALMA). These facts work together to provide very tight constraints on the system. Since the lens is detected by ALMA, its position relative to the lensed images is unambiguous. Also, because there is a strongly lensed source with multiple images, the Einstein radius of the lens is unambiguous. A byproduct of these two facts is that the magnification factor of the weakly lensed source is known to very high precision as well. It experiences a magnification factor of $\mu_{870} = 1.520 \pm 0.002$ despite being located $\approx 4''$ north of the lens (which has an Einstein radius of 1.353 ± 0.005). We use these numbers to inform our estimates of the Einstein radius for weakly lensed sources without the excellent constraints provided by this system. Finally, this source is detected (and unresolved) in the NRAO VLA Sky Survey (Condon et al. 1998), having $S_{1.4\text{ GHz}} = 21.8 \pm 0.8$ mJy. Assuming all of this radio emission originates from the lens, this implies a spectral slope of $\alpha = -0.24$ and is consistent with non-thermal emission from the lens.

CDFS_M1: Two sources are detected by ALMA, both of which are weakly lensed by a foreground galaxy seen in the *HST* image. There is also a 3σ peak coincident with *HST* source that may be an indication that the lens has been detected by ALMA. We do not attempt to model this 3σ peak. We assume an Einstein radius of $0''.5$ for the lens, since larger values predict the existence of counter images that are not seen by ALMA. The second ALMA source is located $\approx 5''$ from the lens and experiences a small but significant magnification of $\mu_{870} = 1.12 \pm 0.02$. Both ALMA sources appear to be detected by IRAC and have similar mid-IR colors, suggesting they lie at the same redshift (see Figure 3).

ECDFS02: This system is very similar to ADFS05, except that here the two ALMA sources are separated by $\approx 0''.4$ rather than $0''.8$ and one source is brighter than the other by a factor of 2. Assuming the two sources have similar mass to light ratios, their brightness ratios indicate major merger rather than minor merger activity. The projected physical distance is $\approx 2 - 3$ kpc, assuming a redshift of $z = 2$ for the ALMA sources. This could be an example of a major merger approaching final

coalescence and experiencing a significant boost in star-formation due to enhancements in the local gas density brought about by tidal forces during the merger.

Elaiss1: Four sources are detected by ALMA, all of which are weakly lensed by a foreground galaxy seen in the *HST* image. We assume an Einstein radius of $1''.5$ for the lens as larger values begin to predict counter images that are not seen by ALMA. The magnification factors reported here should be regarded as upper limits since we do not have strong constraints on the lower limit of the Einstein radius of the lens (e.g., the magnification factor for the source that is directly south of the lens is reported here to have $\mu_{870} = 1.68 \pm 0.06$, but values as small as $1.1\text{--}1.2$ are likely plausible as well). The ALMA sources are all detected by IRAC and their mid-IR colors are similar, suggesting they lie at the same redshift (see Figure 3).

COS01: This system is similar to ADFS07: a single source that is strongly lensed by a foreground galaxy seen in the *HST* image. In fact, the background source is also detected by *HST* as well as Keck/NIRC-II adaptive optics imaging, and a lens model has been published based on these data (Calanog et al. 2014). The morphology of the lensed emission is very different between the Keck and ALMA imaging, suggesting differential magnification is important in this object. The very small sizes of the sources are consistent with this as well ($r_s = 0.023 \pm 0.003''$, Keck and $r_s = 0.055 \pm 0.007''$, ALMA). Adopting a redshift of $z = 2$ for the lensed source implies physical sizes of ≈ 150 pc and ≈ 300 pc for the rest-frame optical and rest-frame FIR, respectively.

COS02: Five sources are detected by ALMA (the brightest of which has already been detected; Smolčić et al. 2012), none of which appear to be lensed. Previous research has shown this to be an overdense region (this object is called COSBO3 in Aravena et al. 2010) with a photometric redshift of $z = 2.3\text{--}2.4$. Our ALMA imaging offers the first convincing evidence that the associated galaxies in the overdensity are sub-mm bright and thus intensely star-forming. There are a number of $2 - 3\sigma$ peaks in the map that could be real. This would further increase the multiplicity rate for this object, but we caution that there are also negative peaks of similar amplitude (i.e., $2 - 3\sigma$) present in this map. Some of the ALMA sources have counterparts detected in the *HST* image, whereas all of the ALMA sources are detected by IRAC (see Figure 3). Their mid-IR colors are similar, providing further evidence that the ALMA sources lie at the same redshift.

XMM01: Three sources are detected by ALMA, all of which are weakly lensed by two foreground galaxies seen in the *HST* and Keck/NIRC-II imaging. The ALMA imaging is broadly consistent with SMA data originally presented in Fu et al. (2013), with two bright sources and a much fainter third source very close to the more southern bright source. We assume Einstein radii of $0''.5$ for both lenses to reproduce the approach used in Fu et al. (2013). This results in magnification factors for the three sources of $\mu_{870} \approx 1.6 - 1.7$, similar to Fu et al. (2013).

XMM02: Two sources are detected by ALMA, both of which are weakly lensed. This system is similar to ADFS02, although the two ALMA sources are much closer and the lens must be less massive in order to avoid producing multiple images of the closest ALMA source.

The fainter ALMA source has a much lower magnification factor than the brighter source ($\mu_{870} = 1.10 \pm 0.01$ vs. $\mu_{870} = 1.63 \pm 0.11$). As with ADFS02, we caution that these magnification factors represent the “maximal lensing” scenario and hence should be considered upper limits. Both ALMA sources are detected by IRAC and have similar mid-IR colors, suggesting they lie at a similar redshift (see Figure 3).

XMM03: One source is detected by ALMA, and it is weakly lensed by two foreground galaxies seen in the *HST* images. We assume an Einstein radius of $1''$ for the foreground lenses and fix the positions of both lenses according to the location of the foreground galaxies in the *HST* image. As with XMM02, this is the “maximal lensing” scenario, so our magnification measurement of $\mu_{870} = 1.80 \pm 0.16$ should be considered an upper limit.

XMM04: Two sources are detected by ALMA, none of which appear to be lensed. The brighter ALMA source is weakly detected in the CFHT *i*-band image.

XMM05: One source is detected by ALMA, and it is weakly lensed by a group of foreground galaxies seen in the *HST* image. We assume an Einstein radius of $0''.2$ for the nearest lensing galaxy and allow a $\pm 0''.4$ shift in its position relative to that indicated by the *HST* image (which has its astrometry tied to SDSS). We represent the remaining members of the group as a single SIS located $4''.5$ south and $4''.5$ east of the image centroid and having an Einstein radius of $2''.0$. This is meant to represent the “maximal lensing” scenario, so our measurement of μ_{870} should be regarded as an upper limit. The presence of two 3σ peaks located near the center of the residual image indicates that the model does not fit the data perfectly. This could be an indication that either of our assumptions for the lens potential or source structure are oversimplifications. Higher resolution imaging is needed to determine the most likely cause.

XMM06: One source is detected by ALMA, and it is strongly lensed by one foreground galaxy seen in the *HST* image. The lensed source is not detected in the *HST* image. This object also has high quality SMA imaging and an accompanying lens model that produces consistent results with those given here (Bussmann et al. 2013).

XMM16: Three sources are detected by ALMA, all of which are weakly lensed by a foreground galaxy detected in the *HST* image and located $\approx 6''$ from the ALMA sources. The central source is much brighter than the other two sources, which makes fitting a model challenging. We forced the positions of the second and third sources to be at least $0''.5$ and $-0''.5$ away from the first source in declination, respectively. Furthermore, we fixed the position of the lens to be located $2''.5$ west and $0''.5$ south of the image centroid given in Table 1. We also fixed the Einstein radius to be $1''.0$, a typical value for isolated galaxies in this sample and in Bussmann et al. (2013). Because the source is so far from the lens, the magnification factor is only $\mu_{870} = 1.19 \pm 0.01$.

XMM101: One source is detected by ALMA, and it appears to be unlensed. A faint smudge seen in the *HST* image of this source is due to a star located $3''.5$ northeast of the ALMA source.

XMM102: Five sources are detected by ALMA, none of which appear to be lensed. There are a few faint smudges seen in the *HST* image which are likely to be the rest-frame optical counterparts to the ALMA sources.

The ALMA sources are all arranged in a chain like shape, possibly suggestive of a larger filamentary overdensity in which they might reside. IRAC imaging provides support for this hypothesis (see Figure 3), as all of the ALMA sources are detected and have similar mid-IR colors (suggesting they lie at similar redshift).

XMM108: One source is detected by ALMA, and it is strongly lensed by one foreground galaxy detected in the Gemini-S image. There is a $\approx 0''.5$ offset in the position of the foreground galaxy between the lens model and the Gemini-S image. Given the absolute astrometric uncertainty of $0''.2$ (based on SDSS), we do not consider this offset to be significant. The presence of a handful of $\pm 3\sigma$ peaks in the residual map is likely an indication that our assumption of a single Gaussian to describe the source morphology is an oversimplification.

XMM109: One source is detected by ALMA, and it is strongly lensed by one foreground galaxy detected in the Gemini-S image. As with XMM108, there is a $\approx 0''.5$ offset between the lens position according to the lens model and the Gemini-S image. We do not consider this offset significant. An alternative model in which the lens is sub-mm luminous cannot be ruled out, but we consider this unlikely for a number of reasons. First, it is a more complex model (having two sources and one lens, rather than one source and one lens). Second, lenses are very rarely detected in sub-mm imaging. Third, the shape and location of the ALMA sources relative to the Gemini-S source are typical of strongly lensed objects (consistent with the very low residuals). Fourth, the alternative lens

model predicts the lensed source to have an intrinsic flux density of ≈ 13 mJy, which would make it the brightest source in the sample.

XMM110: Two sources are detected by ALMA, neither of which are lensed. The faint, diffuse emission seen in the CFHT *i*-band image is atypical of lensing galaxies. The nearest bright galaxy seen at *i*-band is located $\approx 18''$ southeast of the ALMA sources.

XMM115: One source is detected by ALMA, and it is weakly lensed by a foreground galaxy seen in the *HST* image. We assume an Einstein radius of $0''.5$ to represent the “maximal lensing” scenario. Due to the elliptical nature of the lens, this results in a magnification factor of $\mu_{870} = 3.72 \pm 0.42$. The *HST* morphology is complex: diffuse emission to the north of the lens could be a detection of the background source or could be a long spiral arm associated with the lensing galaxy.

XMM119: Two sources are detected by ALMA, both of which are weakly lensed by a foreground galaxy detected in the *HST* image. An Einstein radius of $1''.5$ is used to represent the “maximal lensing” scenario and results in magnification factors of $\mu_{870} = 2.25 \pm 0.17$ and $\mu_{870} = 1.48 \pm 0.09$.

XMM124: One source is detected by ALMA, and it is coincident (within the astrometric uncertainty) with a late-type galaxy seen in the *HST* image. Here, we assume that the *HST* source is the true counterpart to the ALMA source, implying that no lensing is occurring. Consistent with this hypothesis is that the SPIRE photometry show blue colors that suggest this object is at low redshift.

Table 2
Lens properties from parameters of model fits to ALMA sources. Parameters without uncertainties were fixed to the given value.

Short name	Lens ID	RA ₈₇₀ (J2000)	Dec ₈₇₀ (J2000)	σ_{RA} ($''$)	σ_{Dec} ($''$)	θ_E ($''$)	q_{lens}	ϕ_{lens} (deg)
ADFS01	Lens0	04:50:57.688	-53:16:53.10	0.005	0.06	1.0	0.707 ± 0.141	93 ± 7
ADFS02	Lens0	04:50:27.213	-52:41:27.73	0.004	0.06	1.5	0.897 ± 0.047	74 ± 18
ADFS06	Lens0	04:33:40.413	-54:03:39.39	0.009	0.07	0.5	0.662 ± 0.135	37 ± 12
ADFS07	Lens0	04:41:53.867	-54:03:53.23	0.001	0.01	1.006 ± 0.004	0.794 ± 0.008	99 ± 1
ADFS_M0	Lens0	04:38:30.910	-54:18:29.11	0.003	0.12	1.0	0.723 ± 0.068	82 ± 9
CDFS_M0	Lens0	03:27:52.025	-29:09:12.15	0.001	0.01	1.354 ± 0.006	0.955 ± 0.007	80 ± 6
CDFS_M1	Lens0	03:32:10.907	-27:05:32.09	0.002	0.01	0.5	0.807 ± 0.006	176 ± 3
COS01	Lens0	10:01:44.174	+02:57:12.75	0.001	0.02	0.956 ± 0.005	0.775 ± 0.025	72 ± 1
ElaiaS1	Lens0	00:38:23.481	-43:37:01.90	0.013	0.19	1.5	0.790 ± 0.067	44 ± 6
XMM01	Lens0	02:20:16.746	-06:01:42.58	—	—	0.5	0.801 ± 0.062	48 ± 14
—	Lens1	02:20:16.423	-06:01:42.18	—	—	0.5	0.882 ± 0.072	90 ± 17
XMM02	Lens0	02:22:01.671	-03:33:38.45	0.008	0.10	0.5	0.706 ± 0.124	67 ± 11
XMM03	Lens0	02:25:48.129	-04:17:52.20	—	—	1.0	0.531 ± 0.180	45 ± 14
—	Lens1	02:25:47.815	-04:17:48.30	—	—	1.0	0.569 ± 0.197	67 ± 16
XMM05	Lens0	02:30:05.947	-03:41:53.35	0.005	0.06	0.519 ± 0.044	0.852 ± 0.097	24 ± 20
XMM06	Lens0	02:18:30.673	-05:31:31.99	0.001	0.01	0.507 ± 0.004	0.596 ± 0.009	157 ± 1
XMM108	Lens0	02:19:18.398	-03:10:51.31	0.002	0.13	0.928 ± 0.007	0.902 ± 0.024	26 ± 7
XMM109	Lens0	02:29:44.738	-03:41:09.52	0.002	0.01	0.743 ± 0.008	0.703 ± 0.050	26 ± 1
XMM115	Lens0	02:20:21.768	-01:53:30.88	0.002	0.03	0.5	0.547 ± 0.050	11 ± 6
XMM119	Lens0	02:20:29.234	-06:48:46.30	0.005	0.05	1.0	0.663 ± 0.094	64 ± 6

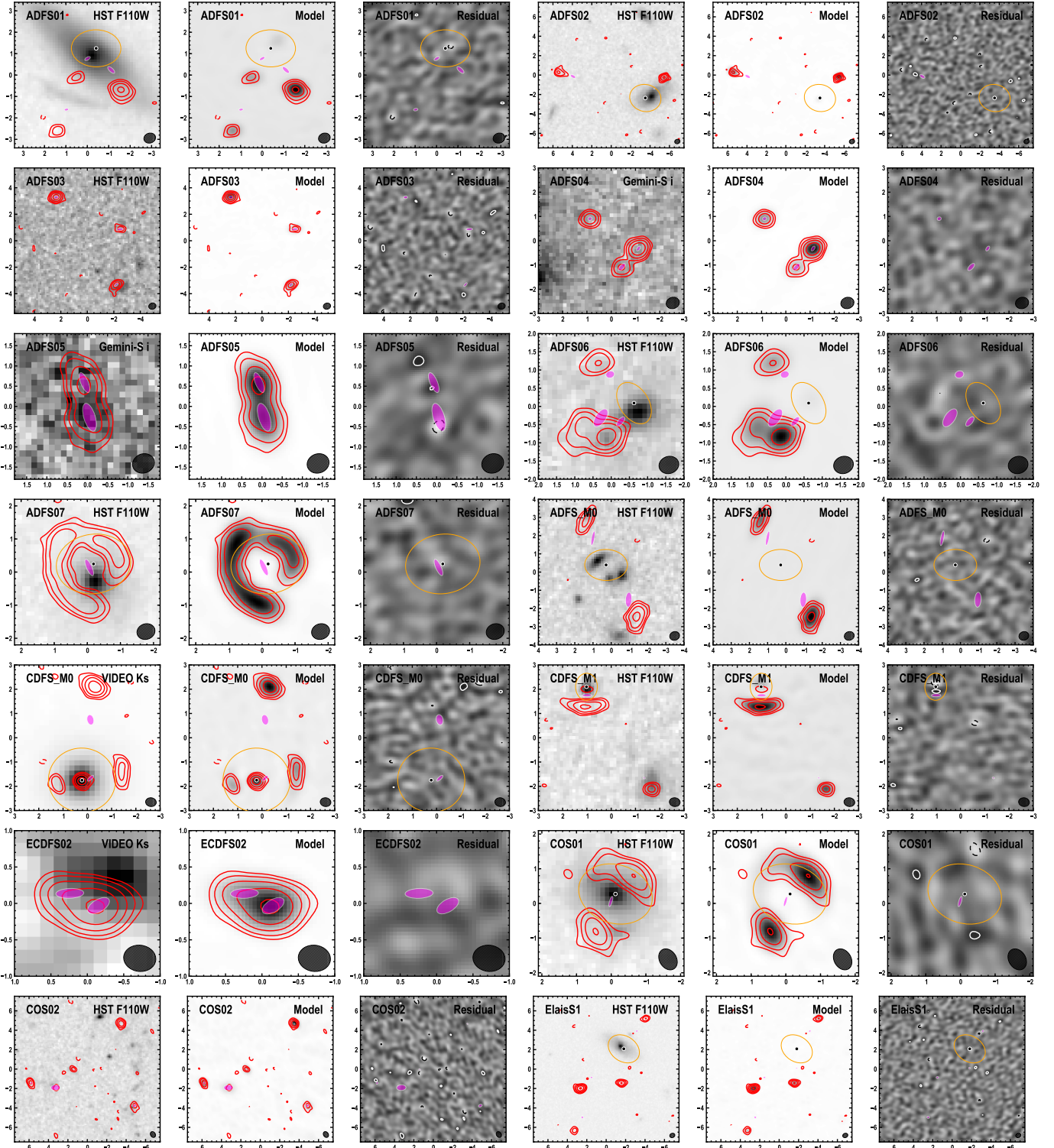


Figure 3. Model fits for each target in the ALMA sample, 3 panels per target. *Left:* ALMA 870 μ m imaging (red contours, starting at $\pm 3\sigma$ and increasing by factors of 2) overlaid on best available optical or near-IR imaging (grayscale, with telescope and filter printed in upper right corner). The location and morphology of all sources used in the model are represented by magenta ellipses. If a lens is present, its location is given by a black circle and its critical curve is traced by an orange line. The FWHM size of the ALMA synthesized beam is shown in the lower left corner of each panel. *Middle:* Same as *left*, but showing best-fit model in grayscale. *Right:* Same as *left*, but showing residual image obtained from subtracting best-fit model from the data.

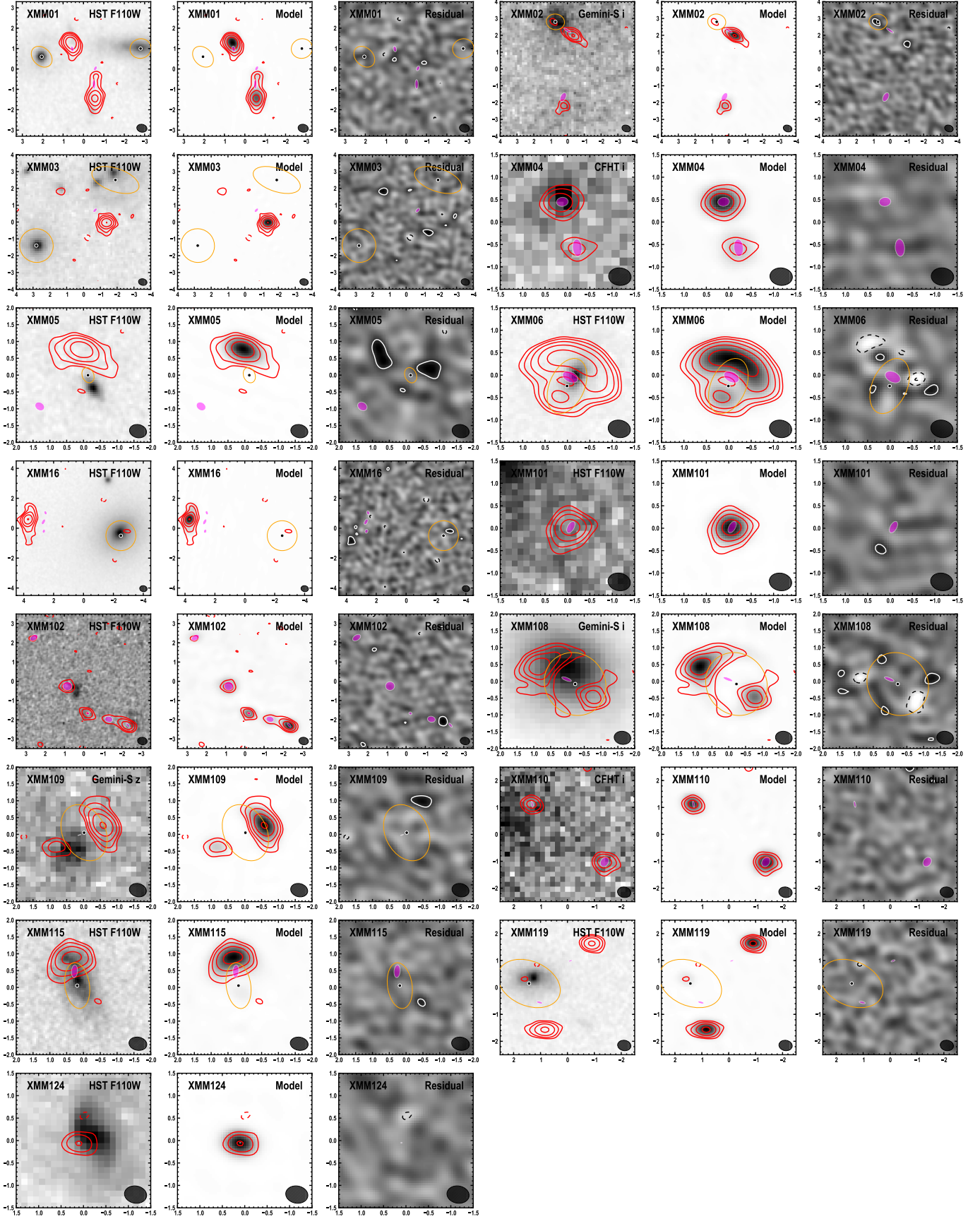


Figure 3. Continued.

Table 3

Intrinsic properties from parameters of model fits to ALMA sources.
 Uncertainties in flux densities do not include absolute calibration uncertainty
 of $\approx 10\%$.

Short name	Source ID	ΔRA_{870} (J2000)	ΔDec_{870} (J2000)	S_{870} (mJy)	r_s ($''$)	q_s	ϕ_s (deg)	μ_{870}
ADFS01	Source0	-0.734 ± 0.069	-1.070 ± 0.053	5.39 ± 0.17	0.112 ± 0.006	0.41 ± 0.05	45 ± 3	1.32 ± 0.16
ADFS01	Source1	1.415 ± 0.056	-2.912 ± 0.059	1.87 ± 0.13	0.059 ± 0.018	0.54 ± 0.12	94 ± 48	1.13 ± 0.07
ADFS01	Source2	0.427 ± 0.055	-0.514 ± 0.059	1.22 ± 0.14	0.084 ± 0.020	0.50 ± 0.13	125 ± 14	1.86 ± 0.43
ADFS02	Source0	-0.868 ± 0.050	0.938 ± 0.048	3.74 ± 0.17	0.055 ± 0.010	0.83 ± 0.09	131 ± 20	1.65 ± 0.32
ADFS02	Source1	7.496 ± 0.058	2.190 ± 0.059	7.28 ± 0.39	0.179 ± 0.012	0.59 ± 0.08	63 ± 6	1.10 ± 0.05
ADFS03	Source0	2.343 ± 0.007	3.284 ± 0.005	7.50 ± 0.24	0.109 ± 0.008	0.70 ± 0.11	92 ± 14	1
ADFS03	Source1	-2.191 ± 0.013	-3.320 ± 0.011	3.84 ± 0.27	0.099 ± 0.019	0.53 ± 0.17	135 ± 24	1
ADFS03	Source2	-2.503 ± 0.035	0.886 ± 0.019	2.06 ± 0.30	0.122 ± 0.040	0.51 ± 0.17	89 ± 20	1
ADFS04	Source0	-1.126 ± 0.005	-0.319 ± 0.004	8.65 ± 0.23	0.073 ± 0.010	0.67 ± 0.15	133 ± 24	1
ADFS04	Source1	0.876 ± 0.011	0.908 ± 0.009	3.53 ± 0.18	0.048 ± 0.019	0.71 ± 0.19	84 ± 43	1
ADFS04	Source2	-0.437 ± 0.017	-1.088 ± 0.016	2.76 ± 0.16	0.093 ± 0.020	0.58 ± 0.20	131 ± 38	1
ADFS05	Source0	0.067 ± 0.008	0.588 ± 0.015	7.02 ± 0.42	0.136 ± 0.012	0.38 ± 0.06	23 ± 5	1
ADFS05	Source1	-0.060 ± 0.009	-0.268 ± 0.018	8.27 ± 0.53	0.193 ± 0.015	0.42 ± 0.06	17 ± 4	1
ADFS06	Source0	0.333 ± 0.101	-0.513 ± 0.040	6.85 ± 0.22	0.091 ± 0.006	0.39 ± 0.05	142 ± 4	1.35 ± 0.17
ADFS06	Source1	0.865 ± 0.123	-0.420 ± 0.041	5.03 ± 0.27	0.165 ± 0.013	0.43 ± 0.06	141 ± 4	1.21 ± 0.10
ADFS06	Source2	0.604 ± 0.108	0.739 ± 0.077	1.99 ± 0.14	0.077 ± 0.015	0.75 ± 0.16	101 ± 40	1.40 ± 0.20
ADFS07	Source0	0.131 ± 0.005	-0.105 ± 0.006	3.17 ± 0.05	0.128 ± 0.005	0.30 ± 0.01	24 ± 1	10.34 ± 0.47
ADFS_M0	Source0	-1.340 ± 0.043	-1.816 ± 0.119	17.51 ± 0.42	0.225 ± 0.006	0.46 ± 0.02	178 ± 1	1.21 ± 0.11
ADFS_M0	Source1	0.658 ± 0.039	1.569 ± 0.111	5.78 ± 0.24	0.180 ± 0.010	0.25 ± 0.02	167 ± 2	1.26 ± 0.13
CDFS_M0	Source0	-0.348 ± 0.006	0.077 ± 0.004	3.61 ± 0.11	0.085 ± 0.004	0.38 ± 0.03	134 ± 3	4.64 ± 1.82
CDFS_M0	Source1	-0.342 ± 0.005	2.489 ± 0.008	11.54 ± 0.18	0.147 ± 0.003	0.65 ± 0.02	14 ± 2	1.26 ± 0.13
CDFS_M0	Source2	0.000 ± 0.000	0.000 ± 0.000	5.83 ± 0.11	0.026 ± 0.009	0.79 ± 0.15	85 ± 63	1
CDFS_M1	Source0	-0.011 ± 0.011	-0.347 ± 0.004	6.02 ± 0.12	0.096 ± 0.005	0.35 ± 0.03	91 ± 2	1.98 ± 0.49
CDFS_M1	Source1	-2.366 ± 0.024	-3.752 ± 0.007	2.51 ± 0.10	0.032 ± 0.012	0.68 ± 0.19	93 ± 55	1.06 ± 0.03
COS01	Source0	0.136 ± 0.011	-0.220 ± 0.016	1.03 ± 0.02	0.068 ± 0.006	0.27 ± 0.04	164 ± 2	14.86 ± 1.90
COS02	Source0	-3.507 ± 0.012	4.659 ± 0.013	3.31 ± 0.16	0.073 ± 0.017	0.70 ± 0.12	94 ± 34	1
COS02	Source1	5.780 ± 0.019	-1.434 ± 0.026	2.26 ± 0.19	0.094 ± 0.029	0.76 ± 0.13	106 ± 65	1
COS02	Source2	-4.869 ± 0.049	-3.769 ± 0.050	1.54 ± 0.23	0.198 ± 0.051	0.65 ± 0.13	72 ± 41	1
COS02	Source3	1.410 ± 0.031	-0.035 ± 0.033	1.45 ± 0.18	0.101 ± 0.042	0.71 ± 0.13	74 ± 42	1
COS02	Source4	3.301 ± 0.083	-1.864 ± 0.060	1.80 ± 0.33	0.312 ± 0.060	0.67 ± 0.13	78 ± 32	1
ECDFDS02	Source0	-0.156 ± 0.011	-0.034 ± 0.011	9.30 ± 1.20	0.099 ± 0.012	0.52 ± 0.12	123 ± 7	1
ECDFDS02	Source1	0.221 ± 0.061	0.127 ± 0.018	4.83 ± 1.26	0.109 ± 0.024	0.38 ± 0.08	88 ± 7	1
ElaisS1	Source0	3.113 ± 0.160	-3.112 ± 0.155	8.02 ± 0.15	0.096 ± 0.005	0.80 ± 0.05	91 ± 6	1.15 ± 0.07
ElaisS1	Source1	-0.111 ± 0.114	-2.172 ± 0.183	3.24 ± 0.12	0.065 ± 0.008	0.84 ± 0.05	87 ± 7	1.34 ± 0.17
ElaisS1	Source2	-1.470 ± 0.158	1.774 ± 0.145	3.27 ± 0.25	0.105 ± 0.016	0.86 ± 0.04	120 ± 7	1.27 ± 0.13
ElaisS1	Source3	4.039 ± 0.165	-7.216 ± 0.174	2.22 ± 0.18	0.124 ± 0.020	0.79 ± 0.05	77 ± 7	1.08 ± 0.04
XMM01	Source0	-1.503 ± 0.013	0.395 ± 0.017	11.61 ± 0.23	0.090 ± 0.005	0.56 ± 0.06	12 ± 19	1.39 ± 0.19
XMM01	Source1	-2.563 ± 0.018	-1.337 ± 0.017	9.56 ± 0.26	0.116 ± 0.006	0.34 ± 0.03	2 ± 1	1.21 ± 0.10
XMM01	Source2	-2.622 ± 0.025	-0.552 ± 0.025	1.45 ± 0.20	0.077 ± 0.025	0.66 ± 0.18	134 ± 33	1.29 ± 0.15
XMM02	Source0	-0.844 ± 0.111	-0.648 ± 0.081	6.24 ± 0.24	0.106 ± 0.007	0.26 ± 0.03	54 ± 2	1.31 ± 0.16
XMM02	Source1	-0.596 ± 0.122	-4.592 ± 0.098	3.38 ± 0.35	0.168 ± 0.023	0.59 ± 0.16	139 ± 41	1.05 ± 0.03
XMM03	Source0	-3.505 ± 0.094	1.937 ± 0.081	12.83 ± 0.31	0.095 ± 0.006	0.59 ± 0.06	142 ± 5	1.40 ± 0.20
XMM04	Source0	0.114 ± 0.009	0.451 ± 0.008	5.46 ± 0.30	0.088 ± 0.012	0.82 ± 0.14	90 ± 44	1
XMM04	Source1	-0.236 ± 0.034	-0.562 ± 0.030	1.78 ± 0.37	0.116 ± 0.051	0.70 ± 0.20	88 ± 55	1
XMM05	Source0	1.520 ± 0.168	-0.683 ± 0.243	9.91 ± 0.24	0.115 ± 0.005	0.72 ± 0.07	69 ± 8	1.57 ± 0.29
XMM06	Source0	-0.278 ± 0.008	0.239 ± 0.011	19.98 ± 0.18	0.122 ± 0.003	0.64 ± 0.02	62 ± 2	3.17 ± 1.08
XMM16	Source0	5.180 ± 0.003	0.924 ± 0.003	12.28 ± 0.24	0.130 ± 0.004	0.53 ± 0.03	-25 ± 2	1.50 ± 0.25
XMM16	Source1	7.560 ± 0.023	2.051 ± 0.028	1.46 ± 0.13	0.093 ± 0.007	0.73 ± 0.11	22 ± 25	1.50 ± 0.25
XMM16	Source2	7.663 ± 0.035	0.755 ± 0.033	1.35 ± 0.12	0.096 ± 0.005	0.73 ± 0.11	-11 ± 37	1.50 ± 0.25
XMM101	Source0	-0.076 ± 0.004	0.024 ± 0.004	8.77 ± 0.24	0.085 ± 0.010	0.52 ± 0.11	152 ± 6	1
XMM102	Source0	-2.308 ± 0.012	-2.275 ± 0.011	5.15 ± 0.32	0.089 ± 0.014	0.63 ± 0.16	58 ± 27	1
XMM102	Source1	0.828 ± 0.025	-0.278 ± 0.023	3.31 ± 0.39	0.137 ± 0.026	0.84 ± 0.10	74 ± 44	1
XMM102	Source2	-0.211 ± 0.017	-1.647 ± 0.014	2.88 ± 0.22	0.058 ± 0.020	0.80 ± 0.13	84 ± 45	1
XMM102	Source3	-1.505 ± 0.157	-1.981 ± 0.064	1.94 ± 0.37	0.283 ± 0.198	0.67 ± 0.17	81 ± 21	1
XMM102	Source4	2.588 ± 0.155	2.611 ± 0.218	0.94 ± 0.18	0.459 ± 0.246	0.58 ± 0.15	96 ± 51	1
XMM108	Source0	0.016 ± 0.238	-0.016 ± 0.283	6.14 ± 0.12	0.074 ± 0.007	0.32 ± 0.02	66 ± 2	4.75 ± 1.87
XMM109	Source0	0.153 ± 0.024	-0.073 ± 0.011	0.84 ± 0.01	0.019 ± 0.003	0.20 ± 0.00	109 ± 1	27.15 ± 4.61
XMM110	Source0	-1.380 ± 0.010	-1.025 ± 0.010	6.31 ± 0.34	0.141 ± 0.011	0.80 ± 0.12	134 ± 36	1
XMM110	Source1	1.311 ± 0.011	1.124 ± 0.010	3.81 ± 0.25	0.070 ± 0.018	0.59 ± 0.22	52 ± 56	1
XMM115	Source0	0.095 ± 0.021	0.442 ± 0.025	8.49 ± 0.20	0.117 ± 0.007	0.52 ± 0.07	-2 ± 5	2.36 ± 0.68
XMM119	Source0	-0.392 ± 0.039	-0.740 ± 0.051	5.51 ± 0.19	0.064 ± 0.006	0.42 ± 0.06	75 ± 5	1.62 ± 0.31
XMM119	Source1	-1.507 ± 0.073	0.805 ± 0.053	5.14 ± 0.15	0.033 ± 0.010	0.46 ± 0.18	116 ± 14	1.24 ± 0.12
XMM124	Source0	0.101 ± 0.011	-0.050 ± 0.009	2.75 ± 0.14	0.020 ± 0.008	0.68 ± 0.20	89 ± 49	1

The combination of our optical or near-IR imaging and our deep, high-resolution ALMA imaging permits us to map the foreground structure along the line of sight to the ALMA sources. With such maps in hand for all of our targets, we can estimate the impact that lensing has

4. RESULTS

4.1. De-lensing the ALMA Sample

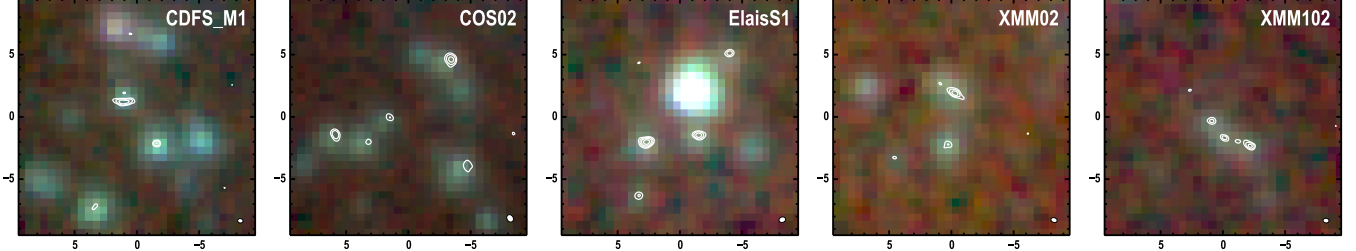


Figure 3. ALMA 870 μm imaging (white contours, starting at 4σ and increasing by factors of 2) overlaid on color composite IRAC imaging (blue = 3.6 μm , green = 4.5 μm , red = 8.0 μm). All panels are 9'.5 on a side. North is up and east is left. The synthesize beam is represented in the lower right corner of each panel. Each of the ALMA counterparts are detected in the IRAC imaging. In addition, the IRAC colors of ALMA sources are broadly consistent, providing some evidence that they are at the same redshift and not physically unassociated blends along the line of sight.

on the intrinsic properties of the ALMA sources. In other words, we can “de-lens” the ALMA sample.

Figure 4 shows the observed (i.e., apparent) and intrinsic (i.e., de-lensed) distributions of S_{870} , r_s , angular separation, and q_s . Here, angular separation is the angular distance between an ALMA source and the centroid of all the ALMA sources for a given *Herschel* DSFG. Lensing has the strongest effect on S_{870} : the median flux density in the ALMA sample drops by a factor of 1.6 when lensing is taken into account, and a two-sided Kolmogorov-Smirnov (KS) test yields a p -value of 0.044. Even if strongly lensed sources are removed from the sample, the median intrinsic flux density is 1.3 times lower than the median apparent flux density. If we only consider examples of weak lensing (i.e., removing the unlensed sources), the factor rises back to 1.6. These factors will be significant sources of error if they are incorrectly ignored. When discussing the intrinsic properties of bright sources discovered in wide-field FIR or mm surveys, it is critical to consider the effects of lensing.

For comparison, we also show the cumulative distribution of S_{870} for the ALESS sample. There is greater overlap in S_{870} between our sample and ALESS than there is in S_{500} (recall Figure 1). This is evidence that the DSFGs in our sample have higher S_{500}/S_{870} ratios than the DSFGs in ALESS. This difference is likely due to differences in dust temperature or redshift distributions of the two samples and likely arises from selection effects.

The effect on the other source parameters (r_s , angular separation, and q_s) is less pronounced. The median source size decreases by a factor of 1.2 in the ALMA sample after accounting for lensing, but the two-sided KS test reveals a p -value of 0.174, suggesting that we cannot rule out the null hypothesis that both size distributions were drawn from the same parent distribution. We find no significant difference between the axial ratios of the apparent and intrinsic distributions as well as between the angular separations of apparent and intrinsic distributions (two-sided KS test p -values of 0.984 and 0.920, respectively).

Finally, the brightest single source in the ALMA sample is XMM16-Source0, with an intrinsic flux density of $S_{870} = 15.42 \pm 0.43$ mJy. However, there are also two objects with multiple sources that have separations smaller than 1'' that have summed flux densities comparable to this: ADFS05 (15.3 mJy) and ECDFS02 (14.1 mJy). This is approaching the values found in the most extreme systems, such as GN20 (20.6 mJy, Pope et al. 2006) and

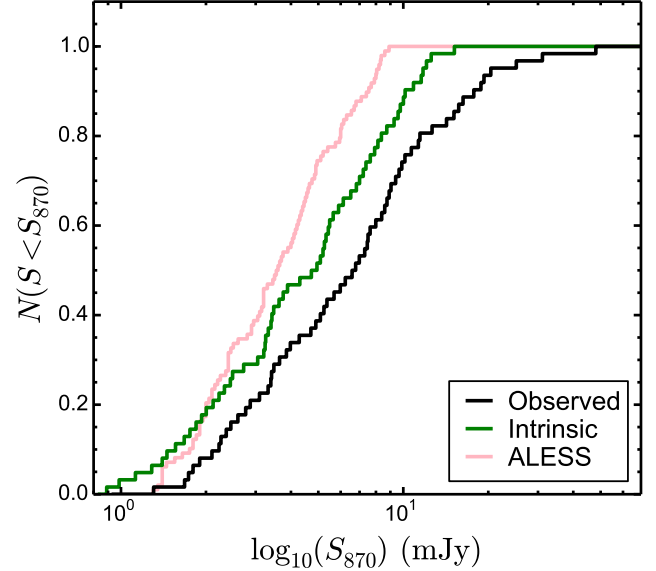


Figure 4. Cumulative distribution functions showing the effect of lensing on the inferred properties of the ALMA sample, including: flux densities (far left panel), effective radii (middle left panel), angular separation from centroid (middle right panel), and axial ratio (far right panel). The median flux density in the ALMA sample drops by a factor of 1.6 when lensing is taken into account. Lensing has a weaker (but still significant) impact on the effective radii and angular separation distributions, but the axial ratio distributions are statistically indistinguishable.

HFLS3 (15-20 mJy; Riechers et al. 2013; Cooray et al. 2014). It is a level that is extremely difficult to reproduce in simulations (e.g., Narayanan et al. 2010). One possibility is that the objects with multiple sources represent blends of physically unassociated systems. Testing this possibility requires redshift determinations of each source and is beyond the scope of this paper.

4.2. Multiplicity in the ALMA Sample

The second key result from our deep, high-resolution ALMA imaging is a firm measurement of the rate of multiplicity in *Herschel* DSFGs. We find that 20/29 *Herschel* DSFGs break down into multiple ALMA sources, implying a multiplicity rate of 69%. However, 5/9 of the single-component systems are strongly lensed. If these five are not considered, then the multiplicity rate increases to 80%. Such a high rate of multiplicity is consistent with theoretical models (Hayward et al. 2013b,a).

In comparison, 69 DSFGs in the MAIN ALESS catalog show a multiplicity rate of 35% - 40% (Hodge et al. 2013). Smoothing our ALMA images and adding noise to

match the resolution and sensitivity of ALESS results in a multiplicity rate of 55% (4 objects with sources that are separated by $< 1''$ become single systems). The redshift distributions for sources selected at S_{500} and S_{870} are expected to be very similar, with only a slightly higher median redshift for the ALESS sample (e.g., $z_{\text{med}} = 2.0$ vs. $z_{\text{med}} = 2.2$; see Zavala et al. 2014). Note though, that our sample has somewhat bluer colors on average than a strictly 500 μm selected sample and is therefore likely to have a slightly lower mean redshift. On the other hand, the ALESS sources are much fainter overall, having a median 870 μm flux density of $S_{870} \approx 6 \text{ mJy}$ compared to $S_{870} = 14.9 \text{ mJy}$ in our ALMA sample. Thus, the evidence favors brighter sources having a higher multiplicity rate. This result is also consistent with multiplicity studies of S_{870} -selected DSFGs by Smolčić et al. (2012) and Barger et al. (2012), who use PdBI/1.1 mm and SMA/870 μm imaging to determine rates of 22% and 40%, respectively.

One useful way to characterize multiplicity is with a comparison of the total 870 μm flux density, S_{total} , with the individual component 870 μm flux density, $S_{\text{component}}$. Figure 5 shows these values for our ALMA sample and compares to ALESS. Lensing has a significant impact on the apparent flux densities of many objects in our ALMA sample, so we are careful to show only intrinsic flux densities in this diagram. This diagram reflects the known result that the multiplicity rate in ALESS rises and the average fractional contribution per component ($\langle S_{\text{component}}/S_{\text{total}} \rangle$) decreases with increasing S_{total} (Hodge et al. 2013). A simple extrapolation of this phenomenon to the flux density regime probed by our ALMA sample would have suggested a very high multiplicity rate and a very low $\langle S_{\text{component}}/S_{\text{total}} \rangle$. We do find a higher multiplicity rate, but we find that $\langle S_{\text{component}}/S_{\text{total}} \rangle$ hovers around 0.4 for essentially the full range in our sample. In other words, the brightest *Herschel* DSFGs comprise 1-3 ALMA components, not 5-10 ALMA components as might have been expected from a naive extrapolation of the ALESS results.

4.3. Spatial Distribution of Multiple Sources

We can dig further into our ALMA data by exploring the average number of ALMA sources per annular area (dN/dA) as a function of how far they are from each other. Figure 6 shows the results of this analysis for both our ALMA sample and ALESS. We formulate the separation as an angular distance between each ALMA source and the centroid of all of the ALMA sources for that *Herschel* DSFG. This is different from Hodge et al. (2013), who use a simple pairwise separation distance estimator, a method that becomes ill-defined when there are more than 2 ALMA counterparts (as is often the case in our ALMA sample). Figure 6 shows dN/dA values for ALESS that have been re-computed using our method. We also show the median and 1σ range found from simulated datasets for both ALESS and our ALMA sample. The simulated datasets consist of 200 runs of DSFGs with the same flux density and multiplicity as the observed datasets (both the ALESS sample and our ALMA sample), but placed randomly within the primary beam FWHM. We also show predictions from simulations by Hayward et al. (2013a) (see below for details).

We recover the result from Hodge et al. (2013) that

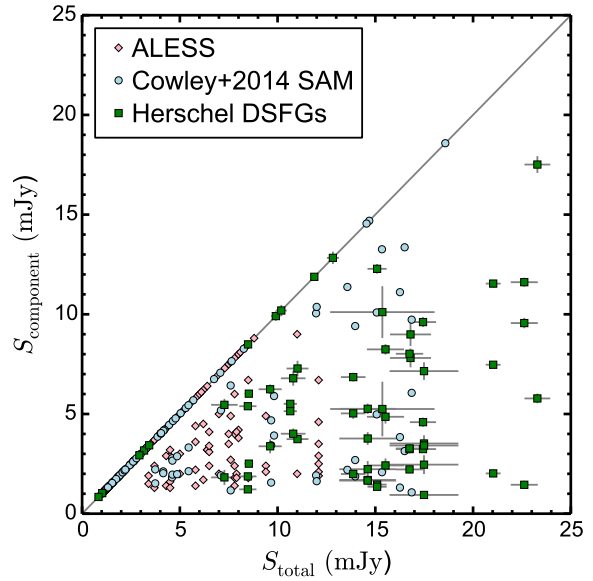


Figure 5. Comparison of the total 870 μm flux density, S_{total} , with the individual component 870 μm flux density, $S_{\text{component}}$ (both of these are after accounting for lensing). Objects falling along the gray dashed line are single component systems (i.e., $S_{\text{total}} = S_{\text{component}}$). The solid lines trace the average ratio of component to total flux for a given total flux. Our sample of *Herschel* DSFGs (ALMA sample, green squares) has a higher multiplicity and a lower $\langle S_{\text{component}}/S_{\text{total}} \rangle$ than the ALESS sample (pink diamonds). This result is consistent with trends within the ALESS sample alone, but the amplitude of the variation is not as large as expected.

the ALESS DSFGs are consistent with a uniformly distributed population. Interestingly, however, there is a dramatic rise in dN/dA for angular separations less than 2'' in our ALMA sample. Indeed, for an angular separation of 0''.5, we find an excess in dN/dA by a factor of ≈ 10 compared to a random, uniformly distributed population. This excess persists (although at significantly lower amplitude) even when the quality of our ALMA observations are degraded to match the typical sensitivity, spatial resolution, and *uv* coverage of ALESS (as represented by observations of ALESS 122). The persistence of the excess suggests that it is an intrinsic property of the sample; i.e., that only the brightest DSFGs show an excess of sources on small separation scales.

An excess of sources with small separations from each other could be a signpost of interacting or merging systems. However, it is also possible that the sources are merely unrelated galaxies that appear blended due to projection effects (Hayward et al. 2013a). Spatially resolved spectroscopy is necessary to answer this question definitely, but is not currently available. Instead, to investigate these possibilities further, we make use of mock catalogs of DSFGs that are based on numerical simulations and presented by Hayward et al. (2013a). We summarize the methodology used to generate dN/dA values from the mock catalogs here and refer the reader to Hayward et al. (2013a) for full details.

Halo catalogs are generated from the *Bolshoi* dark matter-only cosmological simulation (Klypin et al. 2011) using the ROCKSTAR halo finder (Behroozi et al. 2013b,c). Catalogs of subhalos are created from eight randomly chosen lightcones, each with an area of $1.4^\circ \times 1.4^\circ$. Galaxy properties such as stellar mass and SFR are

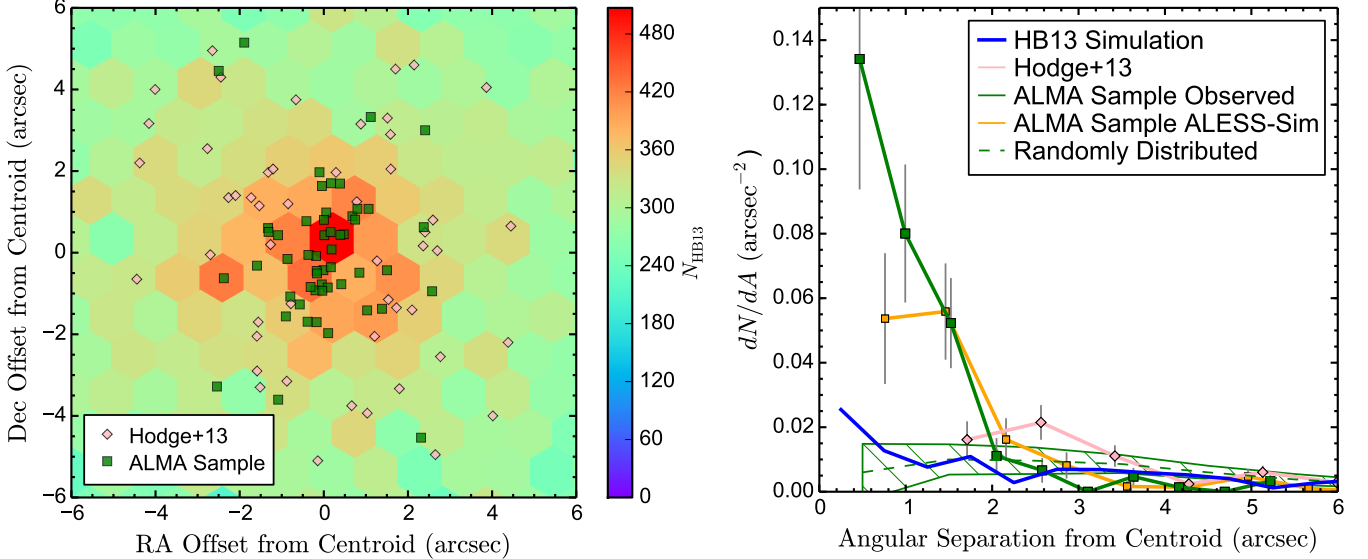


Figure 6. *Left:* Spatial distribution of sources with multiple counterparts found in our ALMA sample (green squares), in ALESS (pink diamonds), and in mock catalogs from Hayward et al. (2013a) (color scale). Sources identified in our ALMA sample lie much closer to each other than they do in either ALESS or the Hayward et al. (2013a) simulations. *Right:* Number of ALMA sources per annular area as a function of angular separation from the ALMA centroid. Results are shown for our ALMA sample (thick green line), ALESS (thick pink line), the Hayward et al. (2013a) simulations (thick blue line), and our ALMA sample as would have been seen with ALESS resolution and sensitivity (thick orange line). We also show the range of separations that would be seen if sources were randomly distributed within the ALMA field of view (green hatched region with solid and dashed green lines). The DSFGs in our ALMA sample show a much stronger excess on angular separation scales $< 2''$ compared to ALESS and the Hayward et al. (2013a) simulations, even when taking into account the difference in sensitivity and spatial resolution between our ALMA observations and those of ALESS.

assigned to the subhalos using the abundance matching method of Behroozi et al. (2013a). Dust masses are assigned using an empirically determined redshift-dependent mass–metallicity relation and an assumed dust-to-metal density ratio of 0.4 (see Hayward et al. 2013b for details). Finally, submm flux densities are interpolated from the SFRs and dust masses using a fitting function that is based on the results of dust radiative transfer calculations performed on hydrodynamical simulations of isolated and interacting galaxies (Hayward et al. 2011, 2012b, 2013b).

A blended source is defined as any galaxy in the mock catalogs above a threshold flux density (S_{thresh}) that has at least one neighbor within a projected angular distance d_{neighbor} . To obtain a direct comparison with our ALMA sample, we use $S_{\text{thresh}} = 1.0 \text{ mJy}$ and $d_{\text{neighbor}} = 40''$. We use the known positions in the mock catalogs for all blended sources and compute centroid and separations for every blended source using the same methodology as we applied to our ALMA sample and to ALESS.

The dN/dA values found in the mock catalogs are shown by the thick blue line in Figure 6. There is a significant increase in dN/dA on separations smaller than $\approx 0''.5$, but the amplitude of the increase is much lower than what is apparent in our ALMA sample.

The Hayward et al. (2013a) model does not include SFR elevations induced by starbursts (see section 4.5 of Hayward et al. 2013a for a detailed discussion of this limitation). To explore whether interaction-induced starbursts are the origin of the excess at small angular separations observed in our ALMA sample, we modified the Hayward et al. (2013a) model to include a crude treatment of interaction-induced SFR elevation. Mock galaxies with one or more neighbors within a physical distance of 5 kpc and with a stellar mass between one-third and

three times that of the galaxy under consideration (i.e. a ‘major merger’) had their SFR increased by a factor of two. For distances smaller than 1 kpc, the imposed increase was a factor of ten. Because these SFR elevations are greater than suggested by simulations (e.g. Cox et al. 2008; Hayward et al. 2011, 2014; Torrey et al. 2012) or observations of local galaxy pairs (e.g. Scudder et al. 2012; Patton et al. 2013), we consider this test to provide an upper limit on the possible effect of interactions on blended sources in the Hayward et al. (2013a) model. We find an insignificant effect on the values of dN/dA when using the merger-induced model as described above. The main reason for this is that only two sources had their SFRs boosted by a factor of ten, and ≈ 150 experienced a factor of two increase. In the Hayward et al. (2013a) model, a factor of two increase in SFR corresponds to only a 30% increase in S_{870} , so it is perhaps unsurprising that the weak boosts in SFR cause little change in dN/dA .

Experiments with stronger interaction-induced SFR elevations showed that very high elevations (e.g. a factor of 10 for separation of 5–15 kpc and 100 for separation of < 5 kpc) in major mergers were required to match the observed excess in dN/dA on small separations. Incorporating starbursts induced by minor-merger could possibly reduce the required SFR elevations. The tension between the model prediction and observations may also indicate that a more sophisticated treatment of blending is necessary.

5. IMPLICATIONS FOR THE BRIGHT END OF THE DSFG LUMINOSITY FUNCTION

The distribution of magnification factors for sources found in wide-field surveys with the brightest apparent flux densities are highly sensitive to the shape of the intrinsic luminosity function at the bright end. In this

section, we combine our ALMA and SMA measurements of magnification factors to investigate this as it pertains to DSFGs.

5.1. Statistical Predictions for μ_{870}

Our methodology follows the procedures outlined in previous efforts to predict magnification factors for DSFGs with a given apparent flux density (chiefly, Lima et al. 2010; Wardlow et al. 2013). We summarize the essential elements here and highlight significant differences where appropriate. Additional details may be found in Fialkov et al. (in prep.).

The key components of the model are the mass density profile of the lenses, $\rho_{\text{lens}}(r)$, the number density of lenses as a function of mass and redshift, $n_{\text{lens}}(M, z)$, the redshift distribution of the sources, dN_{source}/dz , and the intrinsic luminosity function of the sources, $dn_{\text{source}}/dS'_{870}$. The latter component is the least certain component and also has the strongest impact on the predicted apparent luminosity function. For these reasons, we fix all components of the model except the shape of the intrinsic luminosity function. Our goal is to take luminosity functions that can successfully fit observed faint DSFG number counts (Karim et al. 2013) and test whether they lead to predicted magnification factors consistent with our ALMA and SMA observations.

To describe $\rho_{\text{lens}}(r)$, we use a superposition of a singular isothermal sphere (SIS) and a Navarro Frenk White (NFW) profile (Navarro et al. 1997) that is truncated at the virial radius. The NFW profile describes the outskirts of dark matter halos better while the SIS profile is preferred on smaller scales because it correctly fits the observed flat rotational curves in galaxies. We make sure that the resulting probability density of lensing, $P(\mu)$, is normalized to unity.

To describe $n_{\text{lens}}(M, z)$, we generate abundances of halos at each mass and redshift using the Sheth & Tormen (1999) formalism.

To describe dN_{source}/dz , we adopt the following redshift distribution which is based on photometric redshifts of optical counterparts to ALMA sources identified in ALESS (Simpson et al. 2014):

$$dN/dz \propto \frac{1}{a_z \sigma_z \sqrt{2\pi}} \exp\left(\frac{-[\ln(a_z) - \ln(1 + z_\mu)]^2}{2\sigma_z^2 a_z}\right), \quad (2)$$

where $a_z = 1 + z$, $z_\mu = 2.6$, and $\sigma_z = 0.2$.

We explore a variety of intrinsic luminosity functions that are described by either a single Schechter function or a broken-power law. These luminosity functions are selected to represent the range of observed intrinsic luminosity functions for DSFGs which are shown in the left panel of Figure 7 and are drawn from the ALESS survey (Karim et al. 2013) and from interferometric follow-up of the first AzTEC survey in COSMOS (Scott et al. 2008) using the SMA (Younger et al. 2007, 2009) and PdBI (Miettinen et al., in prep.). Interferometric follow-up data in COSMOS (Smolčić et al. 2012) and GOODS-N (Barger et al. 2012) is published, but unknown completeness corrections in the single-dish surveys on which these follow-up datasets are based precludes their usage here.

The Schechter function we use has the usual form

(Schechter 1976):

$$\frac{dn}{dS'} = \frac{n_\star}{S_\star} \left(\frac{S'}{S_\star}\right)^{-\alpha} \exp\left(-\frac{S'}{S_\star}\right), \quad (3)$$

while the broken power-law has the form:

$$\frac{dn}{dS'} = N_\star \left(\frac{S'}{S_\star}\right)^{-\beta_1}, \quad \text{for } S < S_\star, \quad (4)$$

$$\frac{dn}{dS'} = N_\star \left(\frac{S'}{S_\star}\right)^{-\beta_2}, \quad \text{for } S > S_\star.$$

In Table 4, we provide information for three models tested in this paper: the steepest plausible Schechter function, the Karim et al. (2013) broken power-law, and a broken power-law with an even steeper fall-off at higher flux densities than used in Karim et al. (2013).

Table 4
Parameters of DSFG luminosity functions tested in this paper.

Name	n_\star	N_\star	S_\star	α	β_1	β_2
Steep Schechter	424	—	7	1.9	—	—
Karim broken power-law	—	20	8	—	2.0	6.9
Steep broken power-law	—	25	8	—	2	18

The product of the model is the lensing optical depth for a given lensing galaxy and source galaxy. The sum over the distribution of source redshifts and lens masses and redshifts yields the total optical depth for lensing, f_μ . The lensing probability with magnification larger than μ is then calculated via $P(> \mu) = 1 - \exp(-f_\mu)$ and the differential probability distribution is $P(\mu) = -dP(> \mu)/d\mu$. The sum over the distribution of source redshifts and lens masses and redshifts yields the total probability distribution function.

The fundamental measurement provided by the spatially resolved SMA and ALMA imaging and associated lens models is the magnification factor of a source with a given apparent S_{870} . Due to the large size of the combined sample, we can compute the average magnification as a function of S_{870} from the data: $\langle \mu_{870} \rangle$. The same quantity can also be directly computed from our model as:

$$\langle \mu_{870} \rangle = \int_0^\infty \mu P(\mu|S_{870}) d\mu, \quad (5)$$

where the probability for lensing with magnification μ given the apparent flux is:

$$P(\mu|S_{870}) = \frac{1}{N} \frac{P(\mu)}{\mu} \frac{dn}{dS'_{870}} \left(\frac{S_{870}}{\mu}\right), \quad (6)$$

and

$$N = \int \frac{P(\mu)}{\mu} \frac{dn}{dS'_{870}} \left(\frac{S_{870}}{\mu}\right) d\mu. \quad (7)$$

Here dn/dS_{870} is the observed luminosity function and dn/dS'_{870} is the intrinsic luminosity function.

As part of the lens models, the SMA and ALMA imaging also provide the probability that a source with a given apparent S_{870} experiences a magnification above some threshold value, μ_{\min} : $P(\mu > \mu_{\min})$. It is therefore of interest to make a similar prediction from our model. We use the following to do this:

$$P(\mu > \mu_{\min}) = \frac{\int_{\mu_{\min}}^{\infty} P(\mu | S_{obs})}{\int_0^{\infty} P(\mu | S_{obs})}. \quad (8)$$

5.2. Comparing Model with Data

The middle panel of Figure 7 shows a direct comparison of the measured μ_{870} values as a function of apparent S_{870} for the ALMA and SMA samples. We also show a running average of the combined sample (considering only $\mu_{870} > 1.1$ objects, since this is the level at which magnification effects become as significant as absolute calibration uncertainties) to serve as a direct comparison to our theoretical models. We compute this by interpolating the observed μ_{870} and S_{870} onto a fine grid using the Scipy GRIDDATA package and then smoothing the resulting grid using a gaussian filter (specifically, the Scipy GAUSSIAN_FILTER package). Also shown in this diagram are model predictions for the average magnification as a function of S_{870} , $<\mu_{870}>$, assuming the three intrinsic luminosity functions for DSFGs described in Table 4.

At low apparent flux densities ($S_{870} < 10$ mJy), all three models are broadly consistent with each other as well as with the running average of the data, considering the dispersion in the model predictions for μ_{870} at a given S_{870} are $\sigma_{\mu} \approx 1 - 2$ in this regime.

The regime between the low and high apparent flux density limits (10 mJy $< S_{870} < 70$ mJy) is where the three model predictions show the largest difference in $<\mu_{870}>$. The steep rise in the running average in this area is best reproduced by the model with the steep broken power-law luminosity function. However, this model has a difficult time accounting for the low- μ_{870} , high- S_{870} population that comprises about one-third of the sources in this regime. Because the dispersion in the model magnification factors rises smoothly from $\sigma_{\mu} \approx 2$ to $\sigma_{\mu} \approx 8$ over this regime, this difference is significant. The steep Schechter function does a better job of reproducing the low-magnification sources, but it under-predicts the running average over much of the range in S_{870} . Furthermore, there are a number of high- μ_{870} , $S_{870} \approx 10 - 20$ mJy sources that are poorly accounted for by the steep Schechter function. The broken power-law luminosity function advocated in Karim et al. (2013) provides an intermediate result between the steep Schechter function and steep broken power-law and therefore shares some of the strengths and weaknesses of both.

At high apparent flux densities ($S_{870} > 70$ mJy), all of the models over-predict the running average of the magnification. One plausible explanation for this difference is a limitation in the spatial resolution of the observations. In both the ALMA and SMA samples, the spatial resolution is $\approx 0''.5$. This is nearly always sufficient to resolve the images of the lensed galaxy, but it is not always sufficient to resolve the images themselves. Therefore, it may be the case that the lens models over-predict the intrinsic sizes of the lensed galaxies and hence under-predict the magnification factors. If this is true, it would also affect

the intermediate S_{870} regime. A thorough investigation of this possibility is deferred to future work.

One way to deal with this potential limitation in the data is to simplify the quantity of interest. In particular, we next consider the probability of a given source experiencing a magnification above some threshold value, μ_{\min} . As discussed previously, we expect our ALMA and SMA measurements to provide a reliable estimate of this quantity. The results of this are shown in the right panel of Figure 7. We consider two limiting thresholds: $\mu_{\min} = 1.1$ and $\mu_{\min} = 2.0$. The models we consider are the same as those used in the left panel of Figure 7, and our method of creating the running average is also the same.

In the low flux density regime ($S_{870} < 10$ mJy), each model predicts that 10% of sources experience a magnification satisfying $\mu_{870} > 1.1$. This is in disagreement with the data, which show that $\sim 30\%$ of sources in this flux density regime experience $\mu_{870} > 1.1$. The cause of this discrepancy is unclear. One possibility is simply that we are dealing with small number statistics. We speculate that an alternative explanation might be related to the excess number of sources dN/dA found in our ALMA maps with small separations from each other (reported in Section 4.3). Essentially, if the *Herschel* sources have a high multiplicity rate with ALMA counterparts located close to each other, then adding a lens in front of the *Herschel* source will magnify *all* of the ALMA counterparts. If, on the other hand, the ALMA counterparts were located far away from each other, then adding a lens in front of the *Herschel* source would not necessarily cause all ALMA counterparts to be magnified significantly. For this reason, it is plausible that the observed values reported in this figure are biased upwards relative to the simulations outlined in Section 5.1.

In the high flux density regime ($S_{870} > 10$ mJy), all three models as well as the running average in the data show a sharp transition from low probability to high probability of being lensed (for either $\mu_{\min} = 1.1$ or $\mu_{\min} = 2.0$). However, there are major differences in where this transition occurs. For example, the steep Schechter function predicts that 50% of sources with $S_{870} = 50$ mJy have $\mu_{870} < 1.1$. This is inconsistent with the data, which show that all sources with $S_{870} > 50$ mJy have $\mu_{870} > 1.1$. The discrepancy is similar, albeit less severe, for the luminosity function from Karim et al. (2013), where 50% of $S_{870} = 28$ mJy sources are unlensed. In contrast, the very steep broken power-law luminosity function yields a model in which 50% of sources with $S_{870} = 10$ mJy experience $\mu_{870} > 1.1$. This is reasonably consistent with the running average from the data. These results are qualitatively similar if the magnification threshold is increased from $\mu_{\min} = 1.1$ to $\mu_{\min} = 2.0$.

If the steep power-law luminosity function is correct, the implications are significant. We should then expect to find ≈ 1 source satisfying $S_{870} > 10$ mJy in a one square degree survey. This is about a factor of 3 lower than the best-fit model in Karim et al. (2013) and a factor of 7 lower than our steep Schechter function. Moreover, it is a factor of 20 lower than typical measurements from single-dish, broad-beam studies (e.g., Weiβ et al. 2009). This suggests that very luminous galaxies such as GN20 and HFLS3 may be much more rare than previ-

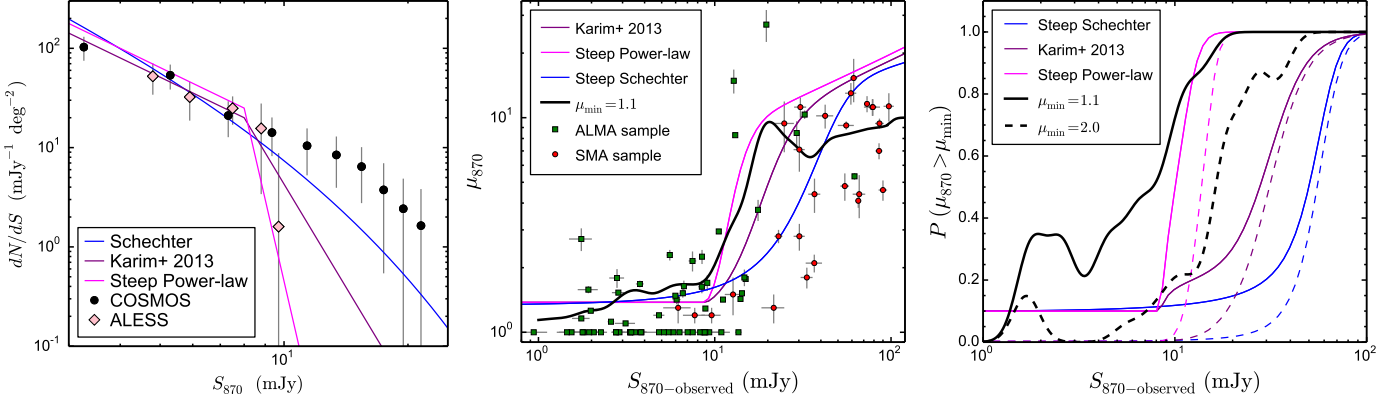


Figure 7. Left: Observed luminosity functions from interferometer follow-up of mm sources in COSMOS (black circles; Younger et al. 2007, 2009, Miettinen et al., in prep.) and from ALESS (pink diamonds; Karim et al. 2013). In comparison, the magenta, purple, and blue lines show three models for the intrinsic luminosity functions of DSFGs. Middle: Magnification factors at 870 μm as a function of apparent S_{870} for every source in our ALMA (green squares) and SMA (red circles) samples. The black line represents a running average of the magnification measurements when sources with $\mu_{870} > 1.1$ are considered. Colored lines show our model predictions $<\mu_{870}>$ for $\mu_{870} > 1.1$ sources for the three intrinsic luminosity functions shown on the left. All three luminosity functions are broadly consistent with the observed magnification factors. Right: Probability that a source with a given S_{870} experiences $\mu_{870} > 1.1$ (solid lines) and $\mu_{870} > 2.0$ (dashed lines). The black lines show the running average from the SMA and ALMA data. Colored lines are the same as in the middle and left panels. The Schechter function predicts too many unlensed or weakly lensed sources with intrinsic flux densities of $S'_{870} \sim 50$ mJy. Our choices for the broken power-law luminosity functions roughly bracket the running average from the data.

ously thought.

6. CONCLUSIONS

We present ALMA 870 μm 0. $''$ 45 imaging of 29 *Herschel* DSFGs selected from 55 deg 2 of HerMES. The *Herschel* sources have $S_{500} = 25 - 130$ mJy, placing them in a unique phase space between the brightest sources found by *Herschel* and those found in ground-based surveys at sub-mm wavelengths that include more typical, fainter galaxies. Our ALMA observations reveal 62 sources down to the 5 σ limit ($\sigma \approx 0.2$ mJy, typically). We make use of optical and near-IR imaging to assess the distribution of intervening galaxies along the line of sight. We introduce a new, publicly available software called UVM-CMFIT and use it to develop lens models for all ALMA sources with nearby foreground galaxy. Our results from this effort are summarized as follows:

1. 36/62 ALMA sources experience significant amplification from a nearby foreground galaxy ($\mu_{870} > 1.1$). The median amplification in the sample is $\mu_{870} = 1.6$. Only 6 sources show morphology typical of strong gravitational lensing and could be identified as lenses from the ALMA imaging alone. A multi-wavelength approach is critical to identifying structure along the line of sight and determining an unbiased measurement of the flux densities in our sample.
2. 20/29 *Herschel* DSFGs break down into multiple ALMA counterparts. Of the 9 isolated systems, 5 are strongly lensed by factors of 5–10. After correcting for amplification, the brightest source in the sample has $S'_{870} = 15.42 \pm 0.43$ mJy. There is a weak trend towards even higher multiplicity at the highest total S_{870} flux densities.
3. When a *Herschel* source comprises multiple ALMA counterparts, these counterparts are located close together. Their separations are much smaller than ALMA counterparts to ALESS sources as well as

simulated sources from Hayward et al. (2013a). This conclusion remains true even when we degrade our ALMA observations to match the spatial resolution, sensitivity, and *uv* coverage of the ALESS observations.

4. Model predictions for the range of magnifications experienced by DSFGs in our sample indicate that a single Schechter function under-predicts the number of lensed sources with apparent $S_{870} > 10$ mJy. Intrinsic luminosity functions with a broken power-law and a very steep decrease above 8 mJy make better predictions for the fraction of lensed sources with $S_{870} > 10$ mJy, but they also predict somewhat higher average magnification factors than are seen in combined sample of ALMA and SMA lens models. This latter result could be explained by limitations in the spatial resolution of the ALMA and SMA imaging, which might lead to the lens models under-estimating the magnification factors.

Our findings suggest that galaxies with intrinsic flux densities above $S'_{870} \approx 10$ mJy are extremely rare. One possible explanation for their rarity is that they are simply the tip of the mass function among starbursts. An alternative is that they represent a very short phase in galaxy evolution. Consistent with this idea is the high multiplicity rate in our ALMA sample as well as the small projected separations between multiple ALMA counterparts. The inability of numerical simulations to reproduce the small projected separations seen in the data might reflect an incomplete theoretical understanding of the enhancement in star-formation by interactions and mergers of galaxies which are already forming stars at a very high rate.

In the future, higher spatial resolution imaging is needed to investigate the morphologies of individual ALMA sources. Tidal tails, multiple nuclei, and other signs of mergers and interactions should become evident at 0. $''$ 1 resolution. In addition, molecular spectroscopy will be critical to determine distances to indi-

vidual ALMA sources and hence characterize what fraction of *Herschel* sources are actually physically associated with each other (and not just a function of projection effects along the line of sight). Molecular spectroscopy will also provide critical information about the inter-stellar medium in these galaxies, yielding insight into the process of how gas turns into stars.

This paper makes use of the following ALMA data: ADS/JAO.ALMA# 2011.0.00539.S. ALMA is a partnership of ESO (representing its member states), NSF (USA) and NINS (Japan), together with NRC (Canada) and NSC and ASIAA (Taiwan), in cooperation with the Republic of Chile. The Joint ALMA Observatory is operated by ESO, AUI/NRAO and NAOJ.

The results described in this paper are based on observations obtained with *Herschel*, an ESA space observatory with science instruments provided by European-led Principal Investigator consortia and with important participation from NASA.

This research has made use of data from the HerMES project (<http://hermes.sussex.ac.uk/>). HerMES is a Herschel Key Programme utilizing Guaranteed Time from the SPIRE instrument team, ESAC scientists, and a mission scientist. HerMES is described in Oliver et al. (2012). The HerMES data presented in this paper will be released through the *Herschel* Database in Marseille (HeDaM¹⁸).

SPIRE has been developed by a consortium of institutes led by Cardiff Univ. (UK) and including: Univ. Lethbridge (Canada); NAOC (China); CEA, LAM (France); IFSI, Univ. Padua (Italy); IAC (Spain); Stockholm Observatory (Sweden); Imperial College London, RAL, UCL-MSSL, UKATC, Univ. Sussex (UK); and Caltech, JPL, NHSC, Univ. Colorado (USA). This development has been supported by national funding agencies: CSA (Canada); NAOC (China); CEA, CNES, CNRS (France); ASI (Italy); MCINN (Spain); SNSB (Sweden); STFC, UKSA (UK); and NASA (USA).

The National Radio Astronomy Observatory is a facility of the National Science Foundation operated under cooperative agreement by Associated Universities, Inc.”

Based on observations obtained at the Gemini Observatory, which is operated by the Association of Universities for Research in Astronomy, Inc., under a cooperative agreement with the NSF on behalf of the Gemini partnership: the National Science Foundation (United States), the National Research Council (Canada), CONICYT (Chile), the Australian Research Council (Australia), Ministério da Ciência, Tecnologia e Inovação (Brazil) and Ministerio de Ciencia, Tecnología e Innovación Productiva (Argentina).

Facilities: ALMA, Gemini-S.

REFERENCES

- Aravena, M., Bertoldi, F., Carilli, C., Schinnerer, E., McCracken, H. J., Salvato, M., Riechers, D., Sheth, K., Smołcić, V., Capak, P., Koekemoer, A. M., & Menten, K. M. 2010, ApJ, 708, L36
- Barger, A. J., Wang, W.-H., Cowie, L. L., Owen, F. N., Chen, C.-C., & Williams, J. P. 2012, ApJ, 761, 89
- Becker, R. H., White, R. L., & Helfand, D. J. 1995, ApJ, 450, 559
- Behroozi, P. S., Wechsler, R. H., & Conroy, C. 2013a, ApJ, 770, 57
- Behroozi, P. S., Wechsler, R. H., & Wu, H.-Y. 2013b, ApJ, 762, 109
- Behroozi, P. S., Wechsler, R. H., Wu, H.-Y., Busha, M. T., Klypin, A. A., & Primack, J. R. 2013c, ApJ, 763, 18
- Blain, A. W. 1996, MNRAS, 283, 1340
- Bothwell, M. S., Smail, I., Chapman, S. C., Genzel, R., Ivison, R. J., Tacconi, L. J., Alaghband-Zadeh, S., Bertoldi, F., Blain, A. W., Casey, C. M., Cox, P., Greve, T. R., Lutz, D., Neri, R., Omont, A., & Swinbank, A. M. 2013, MNRAS, 429, 3047
- Bussmann, R. S., Gurwell, M. A., Fu, H., Smith, D. J. B., Dye, S., Auld, R., Baes, M., Baker, A. J., Bonfield, D., Cava, A., Clements, D. L., Cooray, A., Coppin, K., Dannerbauer, H., Darish, A., De Zotti, G., Dunne, L., Eales, S., Fritz, J., Hopwood, R., Ibar, E., Ivison, R. J., Jarvis, M. J., Kim, S., Leeuw, L. M., Maddox, S., Michałowski, M. J., Negrello, M., Pascale, E., Pohlen, M., Riechers, D. A., Rigby, E., Scott, D., Temi, P., Van der Werf, P. P., Wardlow, J., Wilner, D., & Verma, A. 2012, ApJ, 756
- Bussmann, R. S., Pérez-Fournon, I., Amber, S., Calanog, J., Gurwell, M. A., Dannerbauer, H., De Bernardis, F., Fu, H., Harris, A. I., Krips, M., Lapi, A., Maiolino, R., Omont, A., Riechers, D., Wardlow, J., Baker, A. J., Birkshaw, M., Bock, J., Bourne, N., Clements, D. L., Cooray, A., De Zotti, G., Dunne, L., Dye, S., Eales, S., Farrah, D., Gavazzi, R., González Nuevo, J., Hopwood, R., Ibar, E., Ivison, R. J., Laporte, N., Maddox, S., Martínez-Navajas, P., Michałowski, M., Negrello, M., Oliver, S. J., Roseboom, I. G., Scott, D., Serjeant, S., Smith, A. J., Smith, M., Streblyanska, A., Valiante, E., van der Werf, P., Verma, A., Vieira, J. D., Wang, L., & Wilner, D. 2013, ApJ, 779, 25
- Calanog, J. A., Fu, H., Cooray, A., Wardlow, J., Ma, B., Amber, S., Baes, M., Bock, J., Bourne, N., Bussmann, R. S., Casey, C. M., Chapman, S. C., Clements, D. L., Conley, A., Dannerbauer, H., DeZotti, G., Dunne, L., Dye, S., Eales, S., Farrah, D., Furlanetto, C., Harris, A. I., Ivison, R. J., Maddox, S. J., Magdis, G., Michałowski, M. J., Negrello, M., Nightingale, J., O'Bryan, J. M., Oliver, S. J., Riechers, D., Scott, D., Serjeant, S., Simpson, J., Smith, M., Timmons, N., Thacker, C., Valiante, E., & Vieira, J. D. 2014, ArXiv e-prints
- Capak, P. L., Riechers, D., Scoville, N. Z., Carilli, C., Cox, P., Neri, R., Robertson, B., Salvato, M., Schinnerer, E., Yan, L., Wilson, G. W., Yun, M., Civano, F., Elvis, M., Karim, A., Mobasher, B., & Staguhn, J. G. 2011, Nature, 470, 233
- Carlstrom, J. E. et al. 2011, PASP, 123, 568
- Chapman, S. C., Blain, A. W., Smail, I., & Ivison, R. J. 2005, ApJ, 622, 772
- Condon, J. J., Cotton, W. D., Greisen, E. W., Yin, Q. F., Perley, R. A., Taylor, G. B., & Broderick, J. J. 1998, AJ, 115, 1693
- Conley, A. et al. 2011, ApJ, 732, L35
- Cooray, A., Calanog, J., Wardlow, J. L., Bock, J., Bridge, C., Burgarella, D., Bussmann, R. S., Casey, C. M., Clements, D., Conley, A., Farrah, D., Fu, H., Gavazzi, R., Ivison, R. J., La Porte, N., Lo Faro, B., Ma, B., Magdis, G., Oliver, S. J., Osage, W. A., Pérez-Fournon, I., Riechers, D., Rigopoulou, D., Scott, D., Viero, M., & Watson, D. 2014, ApJ, 790, 40
- Cox, T. J., Jonsson, P., Somerville, R. S., Primack, J. R., & Dekel, A. 2008, MNRAS, 384, 386
- Daddi, E. et al. 2009, ApJ, 694, 1517
- Diolaiti, E., Bendinelli, O., Bonacini, D., Close, L. M., Currie, D. G., & Parmeggiani, G. 2000, in Society of Photo-Optical Instrumentation Engineers (SPIE) Conference Series, Vol. 4007, Society of Photo-Optical Instrumentation Engineers (SPIE) Conference Series, ed. P. L. Wizinowich, 879–888
- Eales, S. et al. 2010, PASP, 122, 499
- Engel, H., Tacconi, L. J., Davies, R. I., Neri, R., Smail, I., Chapman, S. C., Genzel, R., Cox, P., Greve, T. R., Ivison, R. J., Blain, A., Bertoldi, F., & Omont, A. 2010, ApJ, 724, 233
- Foreman-Mackey, D., Hogg, D. W., Lang, D., & Goodman, J. 2013, PASP, 125, 306
- Fu, H. et al. 2013, Nature, 498, 338
- Goodman, J. & Weare, J. 2010, Communications in Applied Mathematics and Computational Science, 5, 65
- Griffin, M. J. et al. 2010, A&A, 518, L3+
- Hayward, C. C., Behroozi, P. S., Somerville, R. S., Primack, J. R., Moreno, J., & Wechsler, R. H. 2013a, MNRAS

¹⁸ <http://hedam.oamp.fr/HerMES>

- Hayward, C. C., Jonsson, P., Kereš, D., Magnelli, B., Hernquist, L., & Cox, T. J. 2012a, MNRAS, 424, 951
—. 2012b, MNRAS, 424, 951
- Hayward, C. C., Kereš, D., Jonsson, P., Narayanan, D., Cox, T. J., & Hernquist, L. 2011, ApJ, 743, 159
- Hayward, C. C., Narayanan, D., Kereš, D., Jonsson, P., Hopkins, P. F., Cox, T. J., & Hernquist, L. 2013b, MNRAS, 428, 2529
- Hayward, C. C., Torrey, P., Springel, V., Hernquist, L., & Vogelsberger, M. 2014, MNRAS, 442, 1992
- Hezaveh, Y. D. et al. 2013, ApJ, 767, 132
- Hinshaw, G., Larson, D., Komatsu, E., Spergel, D. N., Bennett, C. L., Dunkley, J., Nolta, M. R., Halpern, M., Hill, R. S., Odegard, N., Page, L., Smith, K. M., Weiland, J. L., Gold, B., Jarosik, N., Kogut, A., Limon, M., Meyer, S. S., Tucker, G. S., Wollack, E., & Wright, E. L. 2013, ApJS, 208, 19
- Ho, P. T. P., Moran, J. M., & Lo, K. Y. 2004, ApJ, 616, L1
- Hodge, J. A. et al. 2013, ApJ, 768, 91
- Hook, I. M., Jørgensen, I., Allington-Smith, J. R., Davies, R. L., Metcalfe, N., Murowinski, R. G., & Crampton, D. 2004, PASP, 116, 425
- Ivison, R. J., Papadopoulos, P. P., Smail, I., Greve, T. R., Thomson, A. P., Xilouris, E. M., & Chapman, S. C. 2011, MNRAS, 412, 1913
- Ivison, R. J. et al. 2013, ApJ, 772, 137
- Karim, A. et al. 2013, MNRAS, 432, 2
- Keeton, C. R. 2001, ArXiv Astrophysics e-prints
- Klypin, A. A., Trujillo-Gomez, S., & Primack, J. 2011, ApJ, 740, 102
- Le Floc'h, E. et al. 2005, ApJ, 632, 169
- Lilly, S. J., Le Fevre, O., Hammer, F., & Crampton, D. 1996, ApJ, 460, L1
- Lima, M., Jain, B., & Devlin, M. 2010, MNRAS, 406, 2352
- Madau, P., Ferguson, H. C., Dickinson, M. E., Giavalisco, M., Steidel, C. C., & Fruchter, A. 1996, MNRAS, 283, 1388
- Messias, H., Dye, S., Nagar, N., Orellana, G., Bussmann, R. S., Calanog, J., Dannerbauer, H., Fu, H., Ibar, E., Inohara, A., Ivison, R. J., Negrello, M., Riechers, D. A., Sheen, Y.-K., Aguirre, J. E., Amber, S., Birkinshaw, M., Bourne, N., Bradford, C. M., Clements, D. L., Cooray, A., De Zotti, G., Demarco, R., Dunne, L., Eales, S., Fleuren, S., Kamenetzky, J., Lupu, R. E., Maddox, S. J., Marrone, D. P., Michałowski, M. J., Murphy, E. J., Nguyen, H. T., Omont, A., Rowlands, K., Smith, D., Smith, M., Valiante, E., & Vieira, J. D. 2014, A&A, 568, A92
- Narayanan, D., Hayward, C. C., Cox, T. J., Hernquist, L., Jonsson, P., Younger, J. D., & Groves, B. 2010, MNRAS, 401, 1613
- Navarro, J. F., Frenk, C. S., & White, S. D. M. 1997, ApJ, 490, 493
- Negrello, M., Perrotta, F., González-Nuevo, J., Silva, L., de Zotti, G., Granato, G. L., Baccigalupi, C., & Danese, L. 2007, MNRAS, 377, 1557
- Negrello, M. et al. 2010, Science, 330, 800
- Nguyen, H. T. et al. 2010, A&A, 518, L5
- Oliver, S. J. et al. 2012, MNRAS, 424, 1614
- Patton, D. R., Torrey, P., Ellison, S. L., Mendel, J. T., & Scudder, J. M. 2013, MNRAS, 433, L59
- Pilbratt, G. L. et al. 2010, A&A, 518, L1
- Pope, A. et al. 2006, MNRAS, 370, 1185
- Riechers, D. A. et al. 2011a, ApJ, 733, L12
—. 2011b, ApJ, 733, L11+
—. 2013, Nature, 496, 329
- Roseboom, I. G. et al. 2010, MNRAS, 409, 48
- Schechter, P. 1976, ApJ, 203, 297
- Scott, K. S., Austermann, J. E., Perera, T. A., Wilson, G. W., Arétxaga, I., Bock, J. J., Hughes, D. H., Kang, Y., Kim, S., Mauskopf, P. D., Sanders, D. B., Scoville, N., & Yun, M. S. 2008, MNRAS, 385, 2225
- Scudder, J. M., Ellison, S. L., Torrey, P., Patton, D. R., & Mendel, J. T. 2012, MNRAS, 426, 549
- Sersic, J. L. 1968, Atlas de galaxias australes (Cordoba, Argentina: Observatorio Astronomico, 1968)
- Sheth, R. K. & Tormen, G. 1999, MNRAS, 308, 119
- Simpson, J. M., Swinbank, A. M., Smail, I., Alexander, D. M., Brandt, W. N., Bertoldi, F., de Breuck, C., Chapman, S. C., Coppin, K. E. K., da Cunha, E., Danielson, A. L. R., Dannerbauer, H., Greve, T. R., Hodge, J. A., Ivison, R. J., Karim, A., Knudsen, K. K., Poggianti, B. M., Schinnerer, E., Thomson, A. P., Walter, F., Wardlow, J. L., Weiβ, A., & van der Werf, P. P. 2014, ApJ, 788, 125
- Smolčić, V., Aravena, M., Navarrete, F., Schinnerer, E., Riechers, D. A., Bertoldi, F., Feruglio, C., Finoguenov, A., Salvato, M., Sargent, M., McCracken, H. J., Albrecht, M., Karim, A., Capak, P., Carilli, C. L., Cappelluti, N., Elvis, M., Ilbert, O., Kartaltepe, J., Lilly, S., Sanders, D., Sheth, K., Scoville, N. Z., & Taniguchi, Y. 2012, A&A, 548, A4
- Swetz, D. S. et al. 2011, ApJS, 194, 41
- Tacconi, L. J. et al. 2008, ApJ, 680, 246
- Torrey, P., Cox, T. J., Kewley, L., & Hernquist, L. 2012, ApJ, 746, 108
- Treu, T. 2010, ARA&A, 48, 87
- Vieira, J. D. et al. 2013, Nature, 495, 344
- Wardlow, J. L. et al. 2013, ApJ, 762, 59
- Weiβ, A., Kovács, A., Coppin, K., Greve, T. R., Walter, F., Smail, I., Dunlop, J. S., Knudsen, K. K., Alexander, D. M., Bertoldi, F., Brandt, W. N., Chapman, S. C., Cox, P., Dannerbauer, H., de Breuck, C., Gawiser, E., Ivison, R. J., Lutz, D., Menten, K. M., Koekemoer, A. M., Kreysa, E., Kurczynski, P., Rix, H.-W., Schinnerer, E., & van der Werf, P. P. 2009, ApJ, 707, 1201
- Younger, J. D., Fazio, G. G., Huang, J.-S., Yun, M. S., Wilson, G. W., Ashby, M. L. N., Gurwell, M. A., Lai, K., Peck, A. B., Petitpas, G. R., Wilner, D. J., Iono, D., Kohno, K., Kawabe, R., Hughes, D. H., Arétxaga, I., Webb, T., Martínez-Sansigre, A., Kim, S., Scott, K. S., Austermann, J., Perera, T., Lowenthal, J. D., Schinnerer, E., & Smolčić, V. 2007, ApJ, 671, 1531
- Younger, J. D., Fazio, G. G., Huang, J.-S., Yun, M. S., Wilson, G. W., Ashby, M. L. N., Gurwell, M. A., Peck, A. B., Petitpas, G. R., Wilner, D. J., Hughes, D. H., Arétxaga, I., Kim, S., Scott, K. S., Austermann, J., Perera, T., & Lowenthal, J. D. 2009, ApJ, 704, 803
- Zavala, J. A., Arétxaga, I., & Hughes, D. H. 2014, MNRAS, 443, 2384